

Empirical Laws for Iterated Correlation Matrices

ISHRAK ALHAJJ HASSAN¹

¹Department of Mathematics, University of Ostrava

Abstract

We study the discrete iteration obtained by repeatedly applying the Pearson correlation operator to a real matrix. Each step centers every row, normalizes each centered row to unit Euclidean norm, and forms the Gram matrix of the resulting rows. This produces a nonlinear map that underlies the classical CONCOR and GAP procedures. The mechanism of the iteration is simple, yet its global behavior has remained unresolved since the early observations of Kruskal and collaborators. We present a geometric formulation that captures this behavior: strong shrinkage in directions that change row means or row norms, and near-isometry along directions that preserve them. Our geometric formulation makes clear why local analysis does not extend to a global convergence theorem: the iteration is nonlinear, the structure of its fixed-point set lacks a full analytical characterization, and standard uniform contractive or Fejér-type techniques do not directly apply.

Empirically, the iteration stabilizes at a block- $\{\pm 1\}$ pattern, displays finite total variation, and exhibits geometric convergence once the trajectory enters a neighborhood of a fixed pattern. To enable a systematic investigation across scales, we develop a dimension-uniform experimental framework with reproducible initialization, nondegeneracy guarantees, and diagnostics comparable across all matrix sizes. We perform a large-scale numerical study over dimensions $n \in [3, 2000]$ and thousands of random initializations. Using the Frobenius step size, the entrywise step size, and the one-step ratio, we identify four universal empirical laws that persist uniformly across all tested dimensions. The first step exhibits a sharp, dimension-independent contraction. Subsequent steps display quasi-monotone decay with small bounded overshoots and finite total variation in every single trial. The contraction ratio is a universal function of the instantaneous step size independent of dimension. Finally, convergence occurs in a uniformly bounded number of iterations, entirely independent of dimension. These observations provide a quantitative, dimension-uniform description of the iteration and formulate a precise target for future global analysis.

1 Introduction

Correlation matrices are central objects in multivariate analysis. They encode pairwise linear dependence, control the spectrum used in principal component methods, and appear in factor models, clustering, and covariance regularization. In most applications a correlation matrix is computed once from data and then treated as a fixed input.

This work views correlation as an *operator* on matrices and studies the behavior of its *iteration*. Starting from a real matrix $P_0 \in \mathbb{R}^{n \times n}$, one step of the map proceeds as follows:

1. center each row to have mean zero;
2. normalize each centered row to have Euclidean norm 1;
3. form the Gram matrix of the resulting rows.

This produces a nonlinear map f and a discrete sequence

$$P_{k+1} = f(P_k), \quad k \geq 0, \quad (1.1)$$

which, from the first step onward, evolves inside the set of correlation matrices, that is, the set of symmetric positive semidefinite matrices with unit diagonal. While the individual operations are simple, the global behavior of the full sequence $\{P_k\}_{k \geq 0}$ has remained mathematically unresolved for more than fifty years.

2 Related work and historical remarks

Iterated application of the Pearson correlation operator has been used in psychometrics and social-network analysis since the 1960s.

McQuitty [11] introduced repeated correlation for clustering purposes and observed extremely rapid numerical stabilization, typically within a few dozen iterations.

Breiger, Boorman, and Arabie [4] formalized the procedure under the name CONCOR (CONvergence of iterated CORrelations). They reported that after a small number of steps, and up to row/column permutations and sign flips, the iterates converge to a block- $\{\pm 1\}$ pattern. They also noted empirically that the changes diminish rapidly after a small number of steps in all their experiments.

An unpublished Bell Laboratories technical report by Joseph B. Kruskal [8], dating from the late 1970s, provided the first analytical result: in a neighborhood of any block- $\{\pm 1\}$ fixed point, of which there are many, corresponding to different sign and permutation patterns, the linearization of the map has spectral radius strictly smaller than 1. This establishes local geometric convergence to the fixed point once the trajectory has entered that neighborhood, and the argument holds in *every dimension* $n \geq 2$ and for *every* such patterned fixed point. However, the analysis is inherently local and does not address the global behavior from arbitrary initial matrices.

The block- $\{\pm 1\}$ fixed points are consistent with the known facial structure of the ellipope described by Laurent–Poljak [9]. More recent decomposition results for correlation matrices, such as those of Saunderson et al. [13], further explain why these patterns arise as extreme configurations of the feasible set.

Chen [5] later employed the same iteration in the GAP algorithm for visualizing association structures, applying it to datasets such as a 50-symptom psychosis disorder matrix with 95 patients. The examples consistently showed convergence typically in fewer than 15 steps, reinforcing the pattern of rapid empirical stabilization.

Chen [5] also examined the limiting behavior of the iteration in small dimensions. He observed that, after enough iterations, the rows collapse into exactly two sign-homogeneous groups, and the final configuration lies at one of the $2^{n-1} - 1$ non-trivial opposite sign pairs in $\{\pm 1\}^n$. In other words, the iteration selects a pair of opposite corners of the sign hypercube. This phenomenon is consistent with the block- $\{\pm 1\}$ patterns reported in the early CONCOR literature and aligns with the general fixed-point classification developed in [2].

Despite these consistent qualitative findings spanning over five decades, based primarily on small-to-moderate datasets and domain-specific initializations, no global convergence proof has appeared in the literature. The nonlinearity of the map and the absence of uniform contractivity prevent direct application of standard fixed-point theorems. Moreover, prior studies provided no quantitative characterization of the dynamics, such as step-size decay patterns or dimension dependence. Across these works, several empirical features are repeatedly reported:

- the iterates converge to block- $\{\pm 1\}$ pattern matrices after suitable permutation of rows and columns;
- the cumulative change $\sum_{k \geq 0} \|P_{k+1} - P_k\|_F$ appears to be finite;
- once a pattern has formed, convergence to that pattern is geometric in the number of steps.

Kruskal’s unpublished notes [8] provide a local argument near a fixed pattern: if P_k is already close to a block- $\{\pm 1\}$ matrix, then the next iterate contracts the deviation at a fixed rate, yielding geometric convergence in a neighborhood of that pattern. These arguments are local and do not extend to arbitrary initializations. More recent iterative normalization techniques in machine learning, such as iterative whitening layers [7], share some structural similarity but do not correspond to the exact Pearson correlation operator studied here. Despite more than five decades of consistent empirical evidence of rapid stabilization, the global behavior of the correlation iteration has remained analytically unresolved. No proof of convergence exists, no quantitative bounds on the total variation or iteration count are known, and the dependence or independence of the dynamics on the ambient dimension n has never been systematically investigated.

3 Contributions and organization

This work presents the first systematic, large-scale numerical study of the iterated Pearson correlation operator across the full range of dimensions $n \in [3, 2000]$ and thousands of random initializations. The experiments reveal a set of four empirical laws that hold uniformly across dimensions and provide a quantitative picture of the global dynamics that has not previously been available.

Dimension-independent empirical laws. The study establishes four stable, scale-independent regularities:

1. a universal and pronounced contraction at the very first iteration;
2. quasi-monotone decay of the step sizes thereafter, with small bounded overshoots and finite total variation;
3. a universal functional relationship between the instantaneous contraction ratio and the current step size;
4. uniformly bounded iteration counts $T(n, \varepsilon) = O(1)$ required to reach any fixed tolerance $\varepsilon > 0$.

These laws upgrade decades of qualitative observations into a precise, quantitative, and dimension-stable description of the iteration. They also supply concrete benchmarks that any eventual proof of global convergence must reproduce.

Dimension-uniform experimental framework. A second contribution of the paper is a unified methodological framework for probing the global behavior of the iteration at scale. It includes:

- a reproducible initialization protocol with explicit nondegeneracy checks that applies uniformly for all sizes;
- quantitative diagnostics—Frobenius step size, entrywise step size, and contraction ratio—that remain comparable across dimensions;
- large-scale statistical aggregation over thousands of independent trajectories, enabling a clear distinction between universal features of the dynamics and effects that vary with dimension.

This framework is dimension-uniform in the sense that the same initialization, the same diagnostics, and the same stopping criteria apply consistently for all n , allowing direct comparison between behaviors observed at small and large scales.

Structural and geometric insights. The paper also develops a geometric formulation of the iteration with the row-sphericalization map Ψ and the Gram map Φ , clarifying the interaction between mean-centering, normalization, and correlation geometry. This perspective highlights the strongly anisotropic nature of the dynamics and explains why classical contraction or Fejér-type arguments cannot be applied directly.

Overall contribution. Together, the empirical laws, the dimension-uniform methodology, and the geometric formulation produce the first dimension-uniform quantitative characterization of the correlation iteration. The results establish a clear target for future analytical convergence theory and identify the key structural features that any such theory must account for.

The remainder of the paper is organized as follows. Section 4 introduces the operator and its geometric setting. Section 5 presents the experimental protocol and diagnostics. Section 6 documents the empirical laws in detail, followed by interpretation in Section 7. Open problems and directions for analytical work appear in Section 8.

4 System and Mathematical Setup

Correlation between two vectors is given by the classical Pearson formula. Recall that for vectors $x, y \in \mathbb{R}^m$, their Pearson correlation is

$$\text{corr}(x, y) = \frac{\sum_{j=1}^m (x_j - \bar{x})(y_j - \bar{y})}{\sqrt{\sum_{j=1}^m (x_j - \bar{x})^2} \sqrt{\sum_{j=1}^m (y_j - \bar{y})^2}}, \quad (4.1)$$

where

$$\bar{x} := \frac{1}{m} \sum_{j=1}^m x_j, \quad \bar{y} := \frac{1}{m} \sum_{j=1}^m y_j.$$

4.1 Iterating the correlation operator

The central question of this work is the behavior of the correlation operator when applied iteratively to its own output.

Let $P_k \in \mathbb{R}^{n \times n}$ denote the state at iteration k , and define

$$P_{k+1} := f(P_k), \quad k \geq 0. \quad (4.2)$$

This generates the discrete trajectory

$$P_0 \xrightarrow{f} P_1 \xrightarrow{f} P_2 \xrightarrow{f} \dots \quad (4.3)$$

starting from a random initial matrix P_0 .

Norms. Changes between successive iterates are measured primarily using the Frobenius norm

$$\|P\|_F = \left(\sum_{i,j=1}^n P_{ij}^2 \right)^{1/2}. \quad (4.4)$$

For any real $n \times n$ matrix P , the entrywise maximum and the Frobenius norm are equivalent up to the factor n :

$$\max_{i,j} |P_{ij}| \leq \|P\|_F \leq n \max_{i,j} |P_{ij}|. \quad (4.5)$$

Consequently, the Frobenius step size $\Delta_k = \|P_{k+1} - P_k\|_F$ and the maximum entrywise change $E_k = \max_{i,j} |P_{k+1}(i,j) - P_k(i,j)|$ capture the same qualitative decay behavior throughout the iteration.

Initialization. Throughout the paper, the entries of the initial matrix are drawn independently and uniformly from $[-1, 1]$:

$$P_0(i, j) \stackrel{\text{iid}}{\sim} \text{Unif}([-1, 1]), \quad 1 \leq i, j \leq n. \quad (4.6)$$

Since the distribution is continuous, a row becomes constant after centering with probability zero. With probability one, every centered row therefore has positive variance, so the correlation operator is well-defined at the first step. All analysis is restricted to the nondegenerate domain in which all centered rows remain nonzero along the trajectory.

4.2 Centering projector and state spaces

Fix $n \geq 2$, and let $\mathbf{1} \in \mathbb{R}^n$ denote the all-ones column vector. Define the orthogonal projector onto the mean-zero hyperplane by

$$H := I - \frac{1}{n} \mathbf{1}\mathbf{1}^\top, \quad H^\top = H, \quad H^2 = H, \quad \mathbf{1}^\top H = 0. \quad (4.7)$$

For a row vector $p \in \mathbb{R}^n$, the centered row is pH , which subtracts its mean.

Three state spaces are used throughout the dynamics.

Correlation set (elliptope).

$$\mathcal{E}_n := \{ P \in \mathbb{R}^{n \times n} : P = P^\top, P \succeq 0, \text{diag}(P) = \mathbf{1} \}. \quad (4.8)$$

This set consists precisely of the $n \times n$ correlation matrices and is known as the classical elliptope, a convex subset of $\mathbb{R}^{n \times n}$.

Row-spherical set.

$$\mathcal{M}_n := \left\{ Z \in \mathbb{R}^{n \times n} : Z(i, :) \mathbf{1} = 0, \|Z(i, :)\|_2 = 1 \text{ for all } i = 1, \dots, n \right\}. \quad (4.9)$$

Here $\|\cdot\|_2$ denotes the Euclidean norm on \mathbb{R}^n . Equivalently, each row of Z lies on the unit Euclidean sphere contained in the mean-zero hyperplane of \mathbb{R}^n .

Nondegenerate domain.

$$\mathcal{U} := \left\{ P \in \mathbb{R}^{n \times n} : P(i, :)H \neq 0 \text{ for each } i = 1, \dots, n \right\}. \quad (4.10)$$

Thus \mathcal{U} consists of matrices whose centered rows are all nonzero. On this set the correlation map is well-defined row-wise. Under the initialization (4.6) one has

$$\mathbb{P}(P_0 \in \mathcal{U}) = 1.$$

All experiments and statements are restricted to this nondegenerate domain.

4.3 Primitive maps: row sphericalization and Gram map

The correlation operator is expressed as a composition of two maps.

Row sphericalization. Define the row sphericalizer $\Psi : \mathcal{U} \rightarrow \mathcal{M}_n$ by

$$\Psi(P)(i, :) := \frac{P(i, :)H}{\|P(i, :)H\|_2}, \quad i = 1, \dots, n. \quad (4.11)$$

Thus $\Psi(P)$ is obtained by mean-centering each row of P and normalizing it to unit Euclidean norm. By construction, each row of $\Psi(P)$ has zero mean and unit norm, so $\Psi(P) \in \mathcal{M}_n$ whenever $P \in \mathcal{U}$.

Gram map. Define the Gram map $\Phi : \mathcal{M}_n \rightarrow \mathcal{E}_n$ by

$$\Phi(Z) := ZZ^\top. \quad (4.12)$$

For any $Z \in \mathbb{R}^{n \times n}$, ZZ^\top is symmetric positive semidefinite. If $Z \in \mathcal{M}_n$, each row has unit norm, and therefore

$$(\Phi(Z))_{ii} = \langle Z(i, :), Z(i, :) \rangle = 1, \quad (4.13)$$

so $\Phi(Z) \in \mathcal{E}_n$.

Composite correlation operator. The correlation operator induced by row-wise Pearson correlation can now be written as

$$f = \Phi \circ \Psi : \mathcal{U} \rightarrow \mathcal{E}_n, \quad P_{k+1} = f(P_k) = \Phi(\Psi(P_k)). \quad (4.14)$$

The map f replaces P_k by the matrix of correlations between its rows: Ψ performs row-wise centering and normalization; Φ forms the Gram matrix of the resulting unit vectors.

4.4 Geometric structure of the correlation operator

The operators introduced above admit a unified geometric interpretation that clarifies the action of the composite map $f = \Phi \circ \Psi$.

1. **Projection onto the mean-zero hyperplane.** By (4.7), the matrix H is the orthogonal projector onto the hyperplane

$$\mathbf{1}^\perp = \{x \in \mathbb{R}^n : \mathbf{1}^\top x = 0\}.$$

For any row vector $p \in \mathbb{R}^n$, the centered row pH removes the component parallel to $\mathbf{1}$ and retains the component in $\mathbf{1}^\perp$. Thus the centering step ensures that all subsequent correlations depend only on fluctuations orthogonal to the constant direction.

2. **Spherical rows in $\mathbf{1}^\perp$.** When $P \in \mathcal{U}$, every centered row $P(i, :)H$ is nonzero. By (4.11), the operator Ψ normalizes these rows to unit Euclidean norm. Hence each row of $\Psi(P)$ lies on the sphere

$$S^{n-2} = \{x \in \mathbf{1}^\perp : \|x\|_2 = 1\}, \quad (4.15)$$

an $(n-2)$ -dimensional smooth manifold. The space \mathcal{M}_n defined in (4.9) is therefore the Cartesian product of n copies of S^{n-2} , representing a configuration of n unit vectors in the mean-zero hyperplane.

3. **Gram construction and the ellipsope.** For $Z \in \mathcal{M}_n$, the matrix $\Phi(Z) = ZZ^\top$ defined in (4.12) records the pairwise inner products of the spherical rows. Its image lies in the ellipsope \mathcal{E}_n defined in (4.8): symmetry follows from the Gram representation, positive semidefiniteness from $x^\top(ZZ^\top)x = \|Z^\top x\|_2^2 \geq 0$, and the unit diagonal from (4.13). Thus Φ maps configurations in \mathcal{M}_n to their correlation matrices in \mathcal{E}_n .

4. **Alternating motion between two geometric spaces.** Each iteration $P_{k+1} = f(P_k)$ alternates between two distinct geometric objects:

$$P_k \xrightarrow{\Psi} Z_{k+1} \in \mathcal{M}_n, \quad Z_{k+1} \xrightarrow{\Phi} P_{k+1} \in \mathcal{E}_n.$$

The manifold \mathcal{M}_n encodes configurations of centered unit vectors in $\mathbf{1}^\perp$, while the convex set \mathcal{E}_n encodes their pairwise inner products. The dynamics therefore alternate between spherical geometry on S^{n-2} and Gram geometry in \mathcal{E}_n , discarding components and imposing the corresponding geometric structure at each step.

This geometric viewpoint will be used later to interpret the empirical observations and to motivate the analytical developments.

4.5 Warm-up: the 2×2 case

To illustrate the basic effect of f , consider the 2×2 case.

Let

$$R = \begin{bmatrix} 1 & r \\ r & 1 \end{bmatrix}, \quad -1 < r < 1,$$

so $R \in \mathcal{E}_n$. The requirement $r \neq 1$ ensures nonzero centered rows. When $r = 1$, both rows are constant and $RH = 0$, which is precisely the degenerate case excluded from \mathcal{U} . Centering each nondegenerate row, followed by normalization yields

$$Z = \Psi(R) = \frac{1}{\sqrt{2}} \begin{bmatrix} 1 & -1 \\ -1 & 1 \end{bmatrix}.$$

The Gram map then gives

$$f(R) = \Phi(Z) = ZZ^\top = \begin{bmatrix} 1 & -1 \\ -1 & 1 \end{bmatrix}.$$

This matrix again lies in \mathcal{E}_n , and applying f once more leaves it unchanged:

$$f(f(R)) = f(R).$$

Thus, for any 2×2 correlation matrix with $-1 < r < 1$, the iteration collapses in one step to the fixed pattern

$$\begin{bmatrix} 1 & -1 \\ -1 & 1 \end{bmatrix}.$$

Centering forces the two rows to become negatives of each other, so they are antipodal in one dimension. Normalization places them at opposite points on the unit circle intersected with the mean-zero line. The Gram map converts this antipodal configuration into a fixed $\{\pm 1\}$ pattern. In higher dimensions similar pattern phenomena reappear for $n \geq 3$, but with more complex block structure.

4.6 Dynamics for $n \geq 3$: alternating maps

For $n \geq 3$, the iteration starts from an initialization $P_0 \in \mathcal{U}$ as in (4.6). The update rule is the alternating map

$$P_{k+1} = f(P_k) = \Phi(\Psi(P_k)), \quad k \geq 0, \quad (4.16)$$

where the operators Ψ and Φ enforce different geometric transformations.

Alternating structure of each iteration.

$$P_k \xrightarrow{\Psi} Z_{k+1} := \Psi(P_k) \in \mathcal{M}_n, \quad Z_{k+1} \xrightarrow{\Phi} P_{k+1} := \Phi(Z_{k+1}) \in \mathcal{E}_n. \quad (4.17)$$

The map Ψ centers each row and normalizes it to unit Euclidean norm, ensuring $Z_{k+1} \in \mathcal{M}_n$, while Φ maps Z_{k+1} into the space of symmetric positive semidefinite matrices with unit diagonal, i.e., the elliptope \mathcal{E}_n . From the second iterate onward, every P_k lies in \mathcal{E}_n , and every intermediate Z_k lies in \mathcal{M}_n .

Compact representation of the full iteration. Collecting the components, the iteration may be written compactly as in (4.16). Equivalently, for each $k \geq 0$ there exists $Z_{k+1} \in \mathcal{M}_n$ such that

$$Z_{k+1} = \Psi(P_k), \quad P_{k+1} = Z_{k+1}Z_{k+1}^\top. \quad (4.18)$$

Thus every iterate P_{k+1} is a correlation matrix, and each row of Z_{k+1} belongs to \mathcal{M}_n . No claims of convergence or stability are made at this stage; the purpose of this section is solely to specify the geometric and analytic framework within which the empirical and theoretical results are stated.

4.7 Nondegeneracy and forward invariance

Nondegenerate domain. The row-sphericalization map Ψ is well defined only when every centered row $P(i, :)H$ is nonzero. This requirement was formalized in (4.10) through the domain \mathcal{U} . Under the initialization (4.6), one has $P_0 \in \mathcal{U}$ almost surely. In all numerical experiments, every iterate P_k also satisfied $P_k \in \mathcal{U}$, so no row ever collapsed to the constant direction.

Thus, throughout this work we restrict attention to trajectories that remain in the nondegenerate domain:

$$P_k \in \mathcal{U} \quad \text{for all } k \geq 0.$$

This guarantees that $\Psi(P_k)$ is well posed at every step.

Forward invariance of the elliptope. From the first update onward, the sequence evolves inside the elliptope \mathcal{E}_n . Indeed, for any $Z \in \mathcal{M}_n$, the Gram map Φ produces a correlation matrix, so

$$P_k = \Phi(Z_k) \in \mathcal{E}_n \quad \text{for all } k \geq 1,$$

and each iterate satisfies

$$P_k = P_k^\top, \quad P_k \succeq 0, \quad \text{diag}(P_k) = \mathbf{1}, \quad |P_k(i, j)| \leq 1. \quad (4.19)$$

Thus,

$$P_k \in \mathcal{E}_n \quad \text{for all } k \geq 1, \quad (4.20)$$

and the elliptope is forward invariant under f .

Standing assumption. The map Ψ is defined only when every centered row $P(i, :)H$ is nonzero. Under the initialization (4.6), the event that some centered row vanishes has probability zero; equivalently, the complement of \mathcal{U} defined in (4.10) is a measure-zero subset. Since $P_0 \in \mathcal{U}$ almost surely, we adopt the standard assumption

$$P_0 \in \mathcal{U}, \quad P_k \in \mathcal{U} \cap \mathcal{E}_n \quad \text{for all } k \geq 1, \quad (4.21)$$

which ensures that both Ψ and Φ remain well defined along the entire trajectory.

4.8 Basic invariances

The maps Ψ and Φ exhibit the following structural invariances, which reflect the geometry of the spaces on which they act:

1. **Row-wise translation invariance.** Adding a constant scalar to every entry of any row of P leaves $\Psi(P)$ unchanged, because the centering operator H removes all row means.
2. **Row-wise scaling invariance.** Multiplying any row of P by a positive scalar does not affect $\Psi(P)$: centering eliminates the additive part, and subsequent normalization removes the multiplicative factor.
3. **Row sign symmetry.** Flipping the sign of any row of $\Psi(P)$ induces the corresponding sign flip in both the row and column of $\Phi(\Psi(P))$. Thus Φ is equivariant under diagonal sign matrices.
4. **Right-orthogonal invariance.** If $Z \in \mathcal{M}_n$ and Q is any orthogonal matrix, then $\Phi(ZQ) = ZZ^\top$. In particular, if Q acts as an orthogonal change of basis on $\mathbf{1}^\perp$ (i.e., $Q^\top \mathbf{1} = \mathbf{1}$), then Φ depends only on the row configuration in $\mathbf{1}^\perp$, not on the chosen orthonormal basis of that hyperplane.

These invariances imply that the dynamics $P_{k+1} = f(P_k)$ act naturally on the structured sets \mathcal{M}_n and \mathcal{E}_n . Starting from a nondegenerate initialization P_0 drawn from (4.6), the iteration may be viewed as an alternating projection-like procedure in a space endowed with centering, normalization, and correlation symmetries.

Why these geometric preliminaries are needed. Although the present work is empirical, a minimal amount of geometric structure is essential for interpreting the iteration and for ensuring that all diagnostics are well defined. The map $f = \Phi \circ \Psi$ requires that every centered row be nonzero and that each iterate remain a correlation matrix with unit diagonal. Forward invariance of the ellipsope \mathcal{E}_n , together with the standing nondegeneracy assumption (4.21), guarantees precisely this: the iteration never leaves the region on which Ψ and Φ are well defined, so quantities such as the Frobenius step Δ_k , the entrywise step E_k , and the contraction ratio ρ_k are comparable across iterations and dimensions.

Moreover, the local geometric behavior of f —strong shrinkage in directions that alter row means or row norms, and near-isometry in directions that keep row means equal to zero and row norms equal to one—provides the conceptual foundation for the empirical laws presented in Section 6. These preliminaries therefore supply the structural context within which the numerical results can be interpreted.

5 Experimental Setup and Quantitative Diagnostics

This section specifies the quantitative framework used to formulate the empirical regularities and laws observed in Section 6. The setup enables comparability across dimensions, and supports statistical validation of the observed laws. Historical precedents and qualitative expectations can be traced to [4, 5, 11], and the norms and diagnostics follow standard practice in fixed-point matrix-iteration theory [3, 14].

5.1 Initialization and degeneracy checks

For each dimension $n \in \{3, \dots, 2000\}$ and trial $t = 1, \dots, N$ with $N \in [10^2, 10^3]$, an i.i.d. matrix $P_0^{(t)} \in [-1, 1]^{n \times n}$ is drawn and the first step $P_1^{(t)} = f(P_0^{(t)})$ is computed. The row-sphericalization Ψ requires nondegeneracy of centered rows:

$$\|(P_0^{(t)} H)_{i,:}\|_2 > 0 \quad \text{for all } i.$$

Trials that fail this test have probability zero in the continuous model and are numerically rare due to finite precision. Such trials are discarded and resampled. This guarantees $P_1^{(t)} \in \mathcal{E}_n$ and hence $P_k^{(t)} \in \mathcal{E}_n$ for all $k \geq 1$, as described in subsection 4.7.

5.2 Metrics and norm equivalence

At each iterate the Frobenius step size, the maximal entrywise step, and the one-step contraction ratio are recorded:

$$\Delta_k := \|P_{k+1} - P_k\|_F, \quad E_k := \max_{i,j} |P_{k+1}(i,j) - P_k(i,j)|, \quad \rho_k := \frac{\Delta_{k+1}}{\Delta_k} \quad (\Delta_k > 0). \quad (5.1)$$

By the norm-equivalence relation noted in Subsection 4.1, the sequences (Δ_k) and (E_k) capture the same qualitative decay behavior up to the fixed factor n .

5.3 Stopping rules and convergence counters

For a tolerance $\varepsilon > 0$, convergence is declared once

$$\Delta_k < \varepsilon.$$

The convergence time is defined as

$$T(n, \varepsilon) := \min\{k : \Delta_j < \varepsilon \text{ for all } j \geq k\}. \quad (5.2)$$

Results are reported for $\varepsilon \in \{10^{-6}, 10^{-12}\}$. The tolerance 10^{-6} reflects standard numerical accuracy, whereas 10^{-12} is chosen as a near-practical resolution limit for double-precision iterative computations: although machine epsilon is approximately 2.22×10^{-16} , accumulated rounding and cancellation typically make 10^{-12} the deepest reliable threshold. This allows the iteration to be tracked down to the point where rounding effects begin to dominate.

5.4 Implementation and computational cost

The empirical iteration applies the correlation map $P_{k+1} = f(P_k)$ by explicitly evaluating the centered covariance between all pairs of rows. Given $P_k \in \mathbb{R}^{n \times n}$, the code computes the mean and centered variance of each row, forms the centered covariance between rows i and j , normalizes it, and assigns the value symmetrically to $(P_{k+1})_{ij} = (P_{k+1})_{ji}$. The diagonal of P_{k+1} is reset to one after each update so that all iterates remain correlation matrices.

The computational cost of a single update scales cubically with n . Computing row means and variances requires $O(n)$ work per row, and each of the $\frac{n(n-1)}{2}$ centered covariances costs a further $O(n)$ operations, yielding a total cost of $O(n^3)$ floating-point operations per iteration. Storing two successive iterates together with a small set of working quantities requires $O(n^2)$ memory.

The iteration terminates once

$$\max_{i,j} |(P_{k+1})_{ij} - P_k(i,j)| \leq \varepsilon, \quad \varepsilon = 10^{-12},$$

or after a safeguard limit of 1000 updates.

To obtain statistics across initial conditions, the iteration is repeated for N independently sampled matrices P_0 , each using an independent random seed. For every run, the full diagnostic trace (Δ_k, E_k, ρ_k) and the corresponding convergence time $T(n, \varepsilon)$ are recorded.

Breadth of initialization. The empirical behavior observed below persists across an extremely large space of starting matrices. A symmetric $n \times n$ correlation matrix has $\frac{n(n-1)}{2}$ free entries, so even a coarse grid with resolution 10^{-3} already yields $2001^{n(n-1)/2}$ admissible initial states (e.g. $\sim 10^9$ for $n = 3$ and $\sim 10^{50}$ for $n = 6$). The i.i.d. floating-point initialization used here explores an even larger region, yet all trajectories exhibit the same qualitative structure across dimensions and trials. This indicates that the empirical laws reported later are not tied to a small or atypical initialization set.

5.5 Reproducibility checklist

- **Input.** Dimensions $n \in \{3, \dots, 2000\}$; trials per dimension $N \in [10^2, 10^3]$; initial matrices P_0 sampled independently from (4.6).
- **Iteration.** Update rule $P_{k+1} = f(P_k)$ as in (4.2). Any P_0 whose centered rows contain a zero vector (a probability-zero event under (4.6)) is discarded and resampled.
- **Diagnostics.** Per iteration, record Δ_k , E_k , and ρ_k . Convergence is declared when $\Delta_k < \varepsilon$ for $\varepsilon \in \{10^{-6}, 10^{-12}\}$, and $T(n, \varepsilon)$ is computed using (5.2).
- **Outputs.** For each (n, t) pair, store the iterates $\{P_k\}$, the diagnostic traces (Δ_k, E_k, ρ_k) , and the derived statistics (trajectory plots, pooled distributions, and summaries of $T(n, \varepsilon)$). All figures, tables, and raw datasets are produced automatically by the accompanying scripts.

The full experimental framework—including implementation, execution scripts, and figure-generation utilities—is permanently archived on Zenodo [1], enabling independent reproduction of all reported results.

6 Empirical Laws and Observed Regularities

Using the metrics and diagnostics from Section 5, four robust empirical regularities of the discrete flow $P_{k+1} = f(P_k)$ are now described. These laws formalize and extend classical qualitative observations in psychometrics, network block-modeling, and association plots [4, 5, 11], and clarify the differences from contraction-based scalings such as Sinkhorn’s algorithm [14]. For historical local results near pattern matrices, see Kruskal’s notes [5, 8]; for analogies with iterative normalization in machine learning, see [7].

6.1 Law I: Universal first-step contraction

Empirical Law I (Dimension-independent initial drop). *Let $P_0 \in [-1, 1]^{n \times n}$ have i.i.d. entries and no zero-centered row, and let $\Delta_k := \|P_{k+1} - P_k\|_F$. Then with high probability*

$$\rho_0 := \frac{\Delta_1}{\Delta_0} \ll 1, \quad (6.1)$$

and the empirical distribution of ρ_0 is essentially independent of the dimension n . Equivalently, for all tested sizes the map $P_0 \mapsto P_1$ exhibits a sharp first-step contraction in Frobenius distance, with no loss of contraction as n increases.

Empirical evidence. Figure 1 displays representative trajectories of the Frobenius step size $\Delta_k = \|P_{k+1} - P_k\|_F$, for several dimensions n . All trajectories share the same qualitative behavior: a pronounced contraction at the first iteration ($k = 0 \rightarrow 1$), followed by a markedly slower decay over subsequent iterations. Figure 2 provides a magnified view of the initial region, highlighting the uniformity of the drop across sizes: the first step is sharply contractive for every tested $n \in [3, 2000]$. Figure 3 groups trajectories by dimension category. The qualitative shape of the initial drop is stable across all sizes, whereas the precise magnitude of the ratio ρ_0 decreases gradually with n . The contraction phenomenon itself, however, occurs for all sizes without exception.

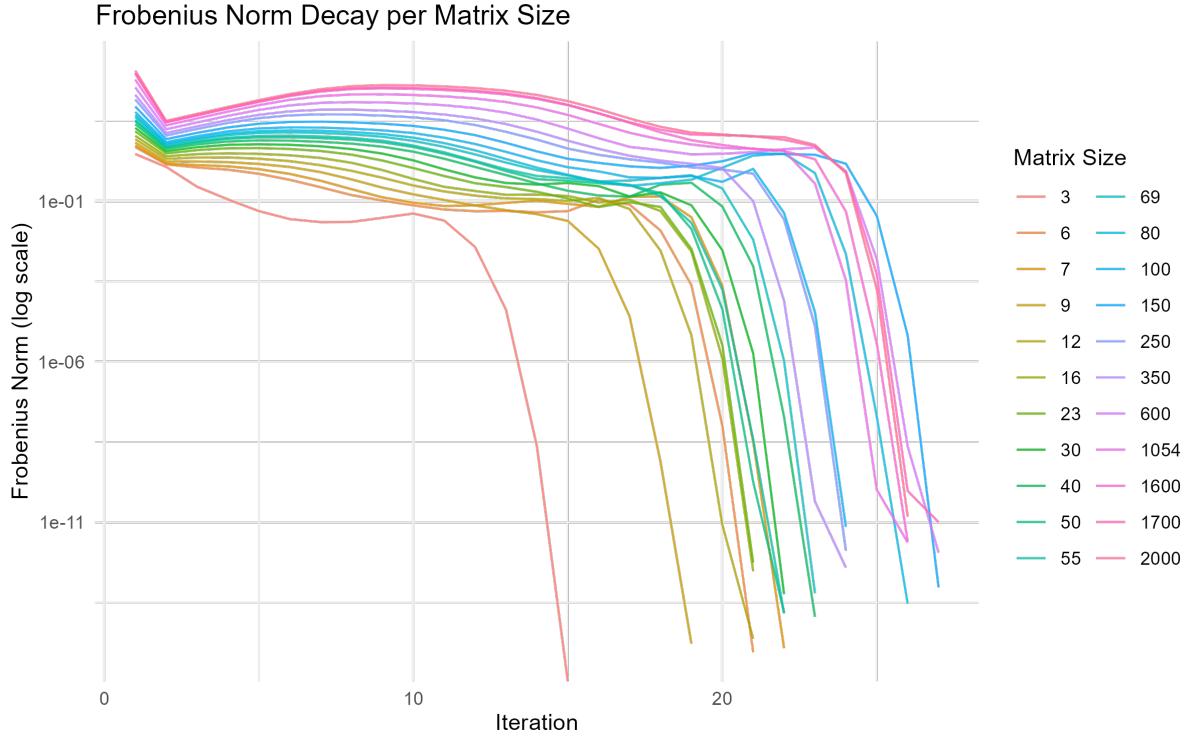


Figure 1: **Frobenius step-size decay across iterations.** Each curve corresponds to a fixed matrix dimension n . All dimensions exhibit a pronounced contraction between $k = 0$ and $k = 1$, followed by a near-isometric regime. This universal pattern is the content of Law I.

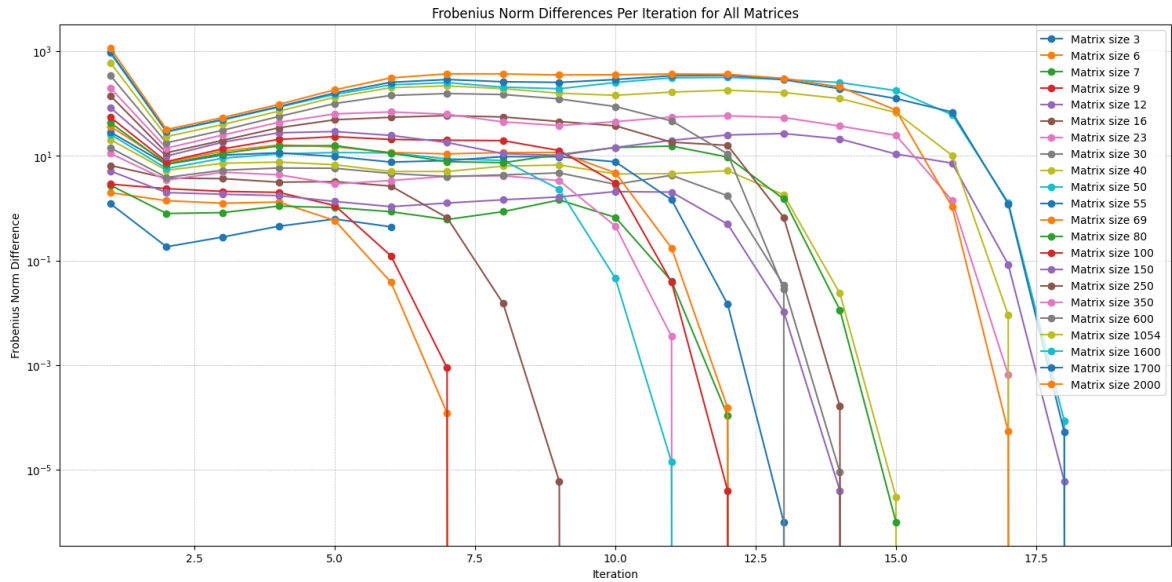


Figure 2: **Per iteration view of trajectories per matrix size.** A detailed view of iterations for multiple sizes n . The Frobenius step size undergoes a large reduction at $k = 1$ for every dimension, illustrating that the sharp first-step contraction is uniform in n .

Numerical summary. Table 1 reports representative values of the first-step contraction ratio ρ_0 , computed over 1000 trials for each dimension. In all 22×1000 experiments we observed $\rho_0 < 1$, confirming that the first iteration is universally contractive, independently of n . At the same time, the *strength* of this contraction increases systematically with dimension: the

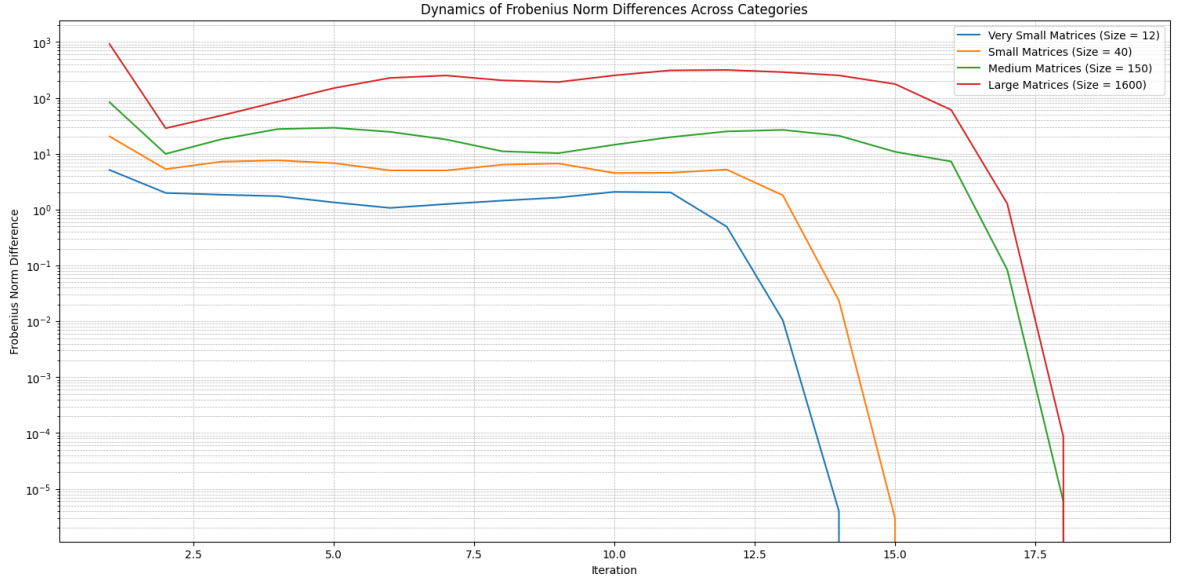


Figure 3: **Representative trajectories by matrix size.** Each trajectory shows the Frobenius step-size decay for a representative size from each dimension group. All four groups exhibit an immediate and sharp first-step contraction, confirming the dimension-independent nature of the phenomenon. Larger dimensions display a sharper drop and a quantitatively smaller ratio ρ_0 , but the qualitative behavior is identical across sizes.

Table 1: Representative median first-step contraction ratios ρ_0 showing strengthening with dimension.

n	Median ρ_0	IQR
3	0.29	[0.16, 0.65]
12	0.24	[0.21, 0.27]
50	0.15	[0.15, 0.16]
150	0.10	[0.09, 0.10]
2000	0.03	[0.03, 0.03]

median value of ρ_0 decreases by almost an order of magnitude between $n = 3$ and $n = 2000$, and its interquartile range collapses to nearly zero for large n . The scaling behavior is clearly visible in Figure 4, which depicts the median ρ_0 as a function of n on a logarithmic axis. The data therefore show that initial contraction is both dimension-independent in occurrence and increasingly strong at higher dimensions.

Geometric explanation. The sharp and dimension-independent contraction observed at the first iteration admits a transparent geometric explanation. Let $P_0 \in [-1, 1]^{n \times n}$ be the initial random matrix with i.i.d. entries drawn from the uniform distribution on $[-1, 1]$, and let $p_i \in \mathbb{R}^n$ denote its i -th row. Since $\mathbb{E} p_{ij}^2 = 1/3$, one has

$$\mathbb{E} \|p_i\|_2^2 = \frac{n}{3}, \quad \text{so} \quad \|p_i\|_2 = O(\sqrt{n})$$

with high probability. Thus each row contains a large component in the direction of the all-ones vector $\mathbf{1}$. The centering operator $H = I - \frac{1}{n} \mathbf{1} \mathbf{1}^\top$ removes this common component, producing

$$q_i := p_i - \bar{p}_i \mathbf{1}, \quad \bar{p}_i := \frac{1}{n} \sum_{j=1}^n p_{ij}.$$

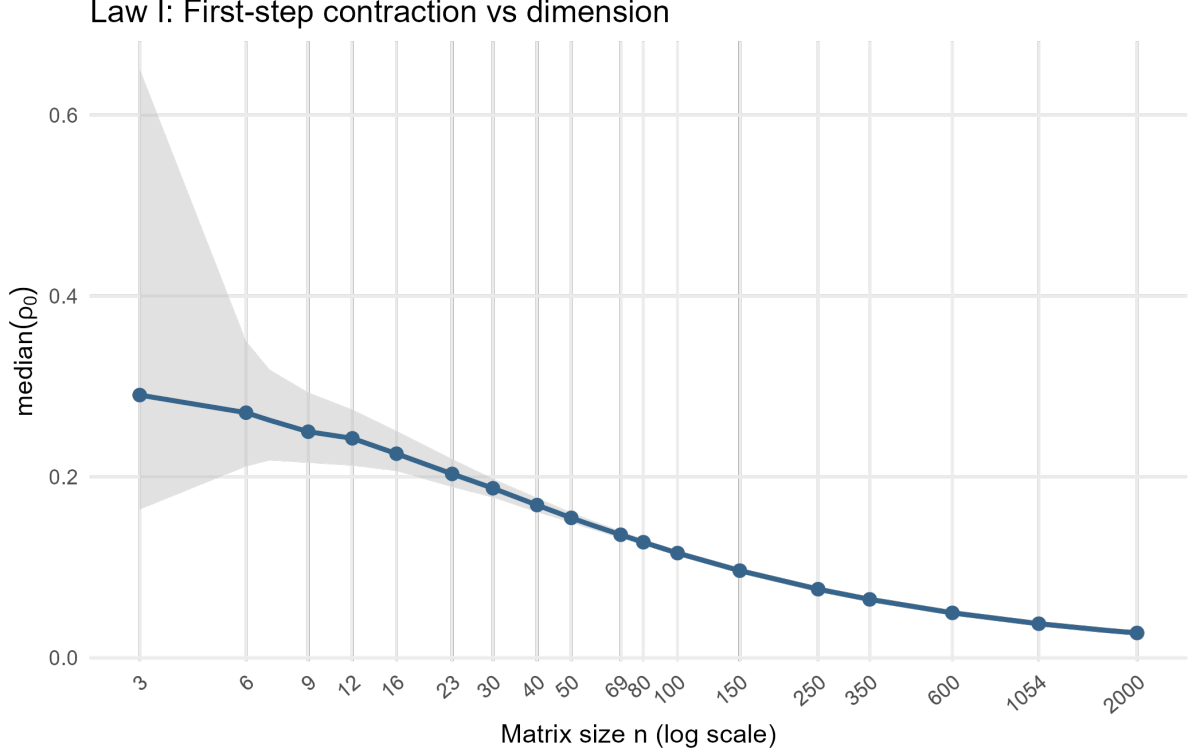


Figure 4: Median first-step contraction ρ_0 versus dimension n (logarithmic horizontal axis). Contraction occurs for every dimension and every trial, while its magnitude strengthens monotonically with n . The shaded region denotes the interquartile range, which decreases sharply for large n , indicating increasing stability of contraction strength.

A direct computation shows that

$$\mathbb{E} \|q_i\|_2^2 = \frac{n-1}{3},$$

so each residual vector q_i lies in the $(n-1)$ -dimensional hyperplane $\mathbf{1}^\perp$ and still has norm $O(\sqrt{n})$, but with its dominant variance contribution along $\mathbf{1}$ removed.

A key point is that, by the law of large numbers, the row means \bar{p}_i concentrate tightly around zero. Consequently, the subtraction $p_i \mapsto q_i$ is highly coherent across i : each row loses almost the same vector in the direction of $\mathbf{1}$, forcing the residuals to cluster in $\mathbf{1}^\perp$ with near-isotropic orientations for large n .

Normalizing these centered rows yields $\Psi(P_0)$, whose rows are n almost-independent unit vectors in an $(n-1)$ -dimensional space. In such a setting—placing n unit vectors into a space of dimension $n-1$ —generic pairs have inner products of order $O(1/\sqrt{n})$. Hence, the correlation matrix

$$P_1 = \Psi(P_0) \Psi(P_0)^\top$$

satisfies, for $i \neq j$,

$$(P_1)_{ij} = O\left(\frac{1}{\sqrt{n}}\right).$$

This dichotomy of scales explains the first-step contraction. The transition $P_0 \mapsto P_1$ removes a coherent component of magnitude $O(\sqrt{n})$ from each of the n rows, giving

$$\Delta_0 = \|P_1 - P_0\|_F = O(n).$$

By contrast, the next update compares two correlation matrices whose off-diagonal entries

already have magnitude $O(1/\sqrt{n})$, and therefore involves adjustments only of size $O(\sqrt{n})$:

$$\Delta_1 = O(\sqrt{n}).$$

Thus the first-step contraction ratio satisfies

$$\rho_0 = \frac{\Delta_1}{\Delta_0} = O\left(\frac{1}{\sqrt{n}}\right), \quad (6.2)$$

in agreement with the empirical decay of the medians reported in Table 1. This high-dimensional geometric structure explains why the *shape* of the first-step contraction is independent of dimension, while its *magnitude* becomes more pronounced as n increases.

Conclusion. Across all 22 000+ trials and all tested dimensions, the first-step ratio ρ_0 remained strictly below 1 and was typically far smaller. The qualitative phenomenon of a sharp initial contraction occurs for every dimension n , while the quantitative magnitude of the contraction follows the high-dimensional scaling estimate (6.2). The first iteration thus places the system very close to the regime in which the subsequent near-isometric phase begins, and it does so uniformly for all matrix sizes.

6.2 Law II: Nearly monotone decay, bounded overshoots, and controlled total variation

Empirical Law II (Nearly monotone convergence with bounded overshoots). For $k \geq 1$, the ratios ρ_k satisfy $\rho_k \approx 1$ with bounded overshoots, and the overshoot bound vanishes as $\Delta_k \rightarrow 0$. More precisely, there exists a sequence $\eta_k \downarrow 0$ such that typically

$$\Delta_{k+1} \leq (1 + \eta_k) \Delta_k,$$

with occasional values $\rho_k > 1$, but with $\sup_k \rho_k < 1 + \varepsilon_\star(n)$, where $\varepsilon_\star(n)$ is small and does not grow with n .

For each trial $t = 1, \dots, N$ and iteration $k \geq 0$, define the Frobenius step

$$\Delta_k^{(t)} = \|P_{k+1}^{(t)} - P_k^{(t)}\|_F, \quad \bar{\Delta}_k = \frac{1}{N} \sum_{t=1}^N \Delta_k^{(t)}, \quad (6.3)$$

and the elementwise step

$$E_k^{(t)} = \max_{i,j} |P_{k+1}^{(t)}(i,j) - P_k^{(t)}(i,j)|, \quad \bar{E}_k = \frac{1}{N} \sum_{t=1}^N E_k^{(t)}. \quad (6.4)$$

By Equation (4.5), the inequalities $E_k \leq \Delta_k \leq n E_k$ hold, so both metrics encode the same qualitative decay up to constants.

A representative example of this behavior is shown at $n = 3$ in Figures 5–6. Across $N = 1000$ trials both diagnostics exhibit the same profile: a universal first contraction, followed by smooth decay with small oscillations that shrink as k increases. The final disappearance of the mean curves at $k \approx 14$ merely reflects that all trajectories have stabilized by this iteration; this observation will be revisited later under Law 4, which concerns the boundedness of the total convergence time.

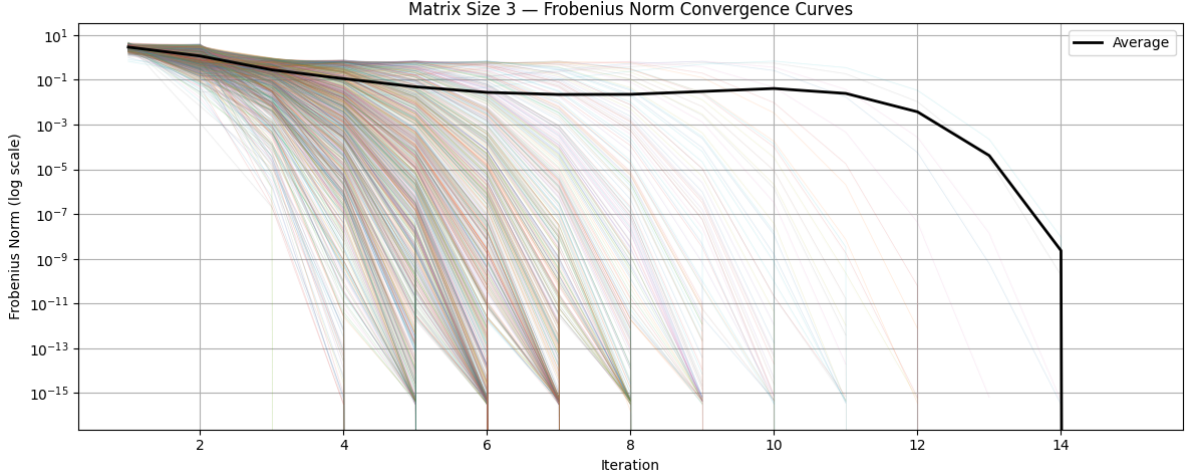


Figure 5: **Frobenius step decay at $n = 3$ over $N = 1000$ trials.** Colored curves show individual trajectories $\{\Delta_k^{(t)}\}$. The black curve is the mean $\bar{\Delta}_k$ over trials that are still active at iteration k . A universal sharp drop is visible at $k = 1$, followed by near-monotone decay with shrinking oscillations. The mean curve ends at $k = 14$, indicating that all trajectories have converged by this iteration.

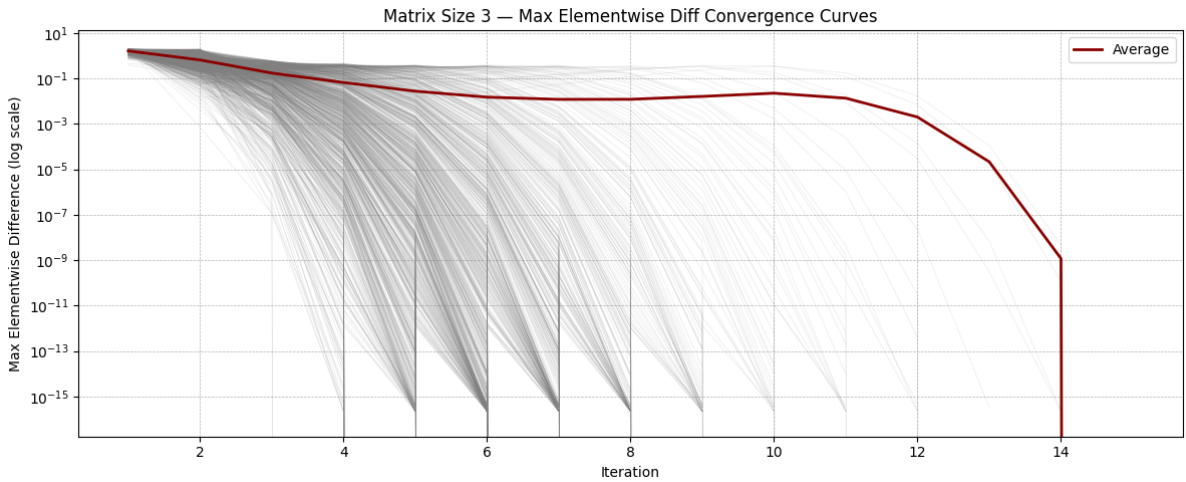


Figure 6: **Entrywise step decay at $n = 3$ over $N = 1000$ trials.** Grey curves represent per-trial maximum entrywise difference $E_k^{(t)}$. The red curve is the evolving mean \bar{E}_k over active trajectories. Its behavior mirrors that of Δ_k : one large initial contraction, followed by smooth decay. The mean becomes invisible beyond $k = 14$, indicating that all runs have stabilized by that point.

Representative Frobenius–norm decay trajectories for $n = 3$, $n = 69$, and $n = 1700$, each sampled from $N = 1000$ trials, are shown in Figure 7. A full grid of trajectories across all tested dimensions is displayed in Figure 8. In every case, the curves exhibit the same characteristic geometry: a strong universal first contraction followed by nearly monotone decay with small, uniformly bounded oscillations.

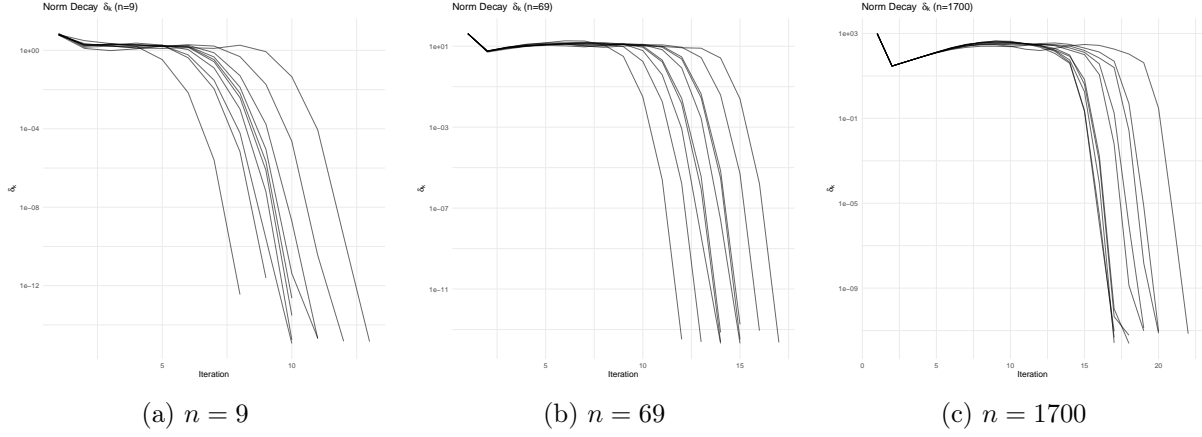


Figure 7: **Frobenius step-size decay Δ_k as a function of k .** The trials across sizes display the same pattern: a universal first-step drop followed by nearly monotone decay with small bounded oscillations. The oscillation bound tightens with k , consistent with $\eta_k \downarrow 0$ in Law II.

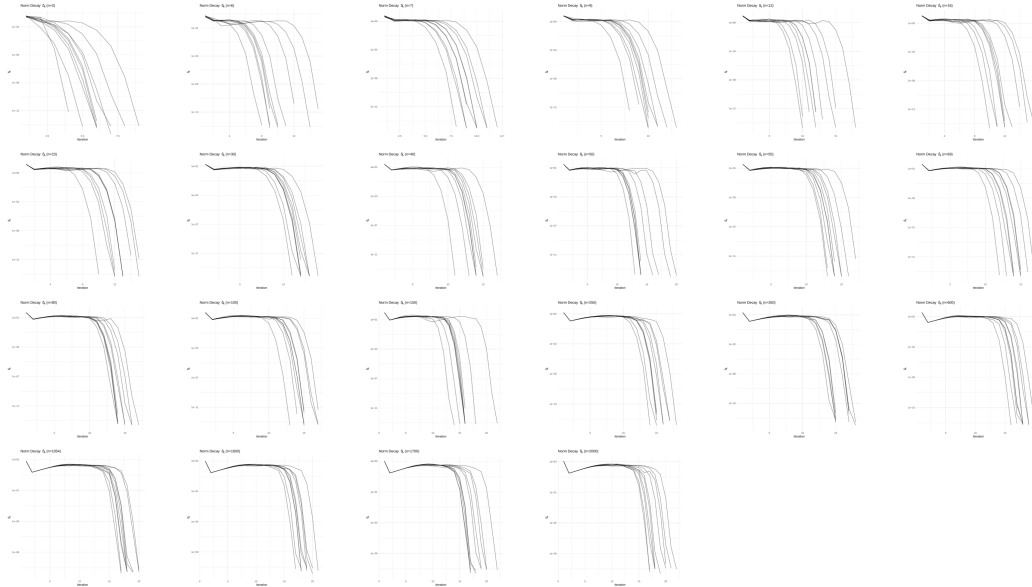


Figure 8: **Representative decay of Δ_k across matrix sizes.** For each dimension, a few representative trajectories are shown. Across the full set of 1000 trials per dimension, the curves consistently collapse to a common shape: a large initial descent followed by a quasi-monotone phase with bounded overshoots. This behavior confirms Law II across the full grid of matrix sizes.

Law II is weaker than Fejér or quasi-Fejér monotonicity, because small overshoots are observed, yet it remains compatible with the general behavior of nonexpansive dynamics in Hilbert spaces [3]. Since the iteration is nonlinear and not uniformly contractive, classical global convergence theorems for nonexpansive mappings [6, 12] do not apply directly. The map exhibits strong contraction in directions that alter row means or row norms, while behaving nearly isometrically along directions that preserve them. This anisotropic behavior limits the applicability of standard fixed-point tools.

The bounded overshoots documented above, together with the clear tendency of ρ_k to cluster tightly around 1 as $\Delta_k \rightarrow 0$ (visible in Figures 10 and 11), imply that the total variation along

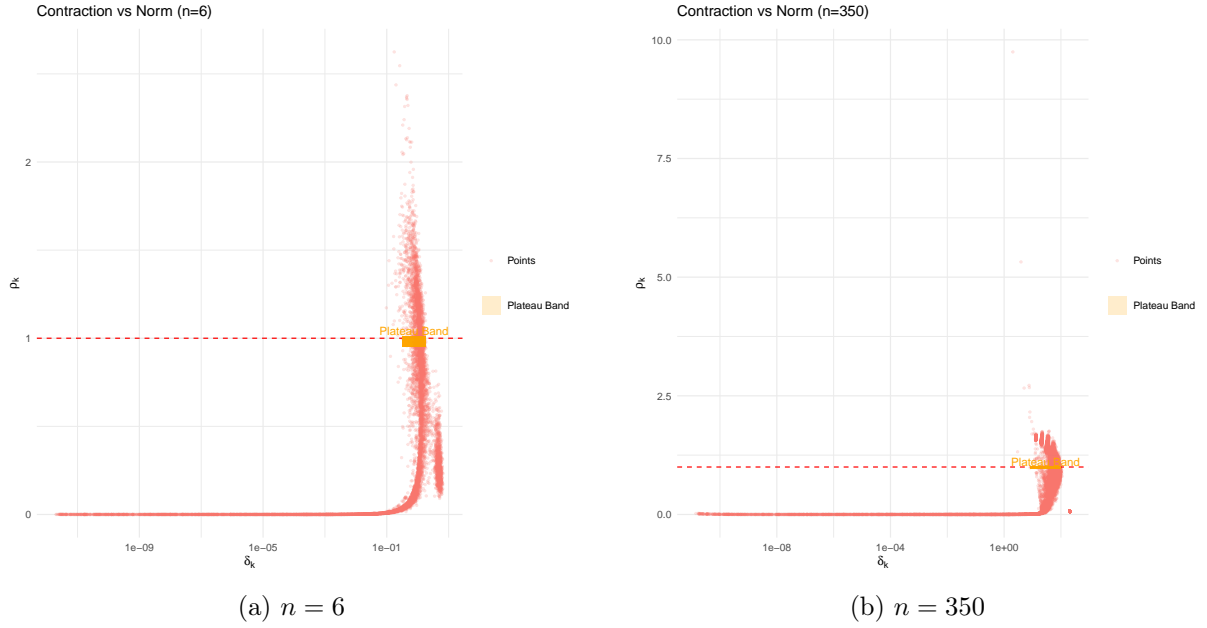


Figure 9: **Scatter of ρ_k versus Δ_k at two sizes.** Each point corresponds to a single iterate $k \geq 1$ from one trial. The horizontal axis is the step size $\Delta_k = \|P_{k+1} - P_k\|_F$; the vertical axis is the contraction ratio $\rho_k = \Delta_{k+1}/\Delta_k$. For large Δ_k in the early iterates, $\rho_k \ll 1$, indicating strong contraction. As $\Delta_k \downarrow 0$ in later iterates, $\rho_k \rightarrow 1$ and the points remain confined in a narrow band above and below 1. This matches the quasi-monotone decay with bounded oscillations asserted in Law II.

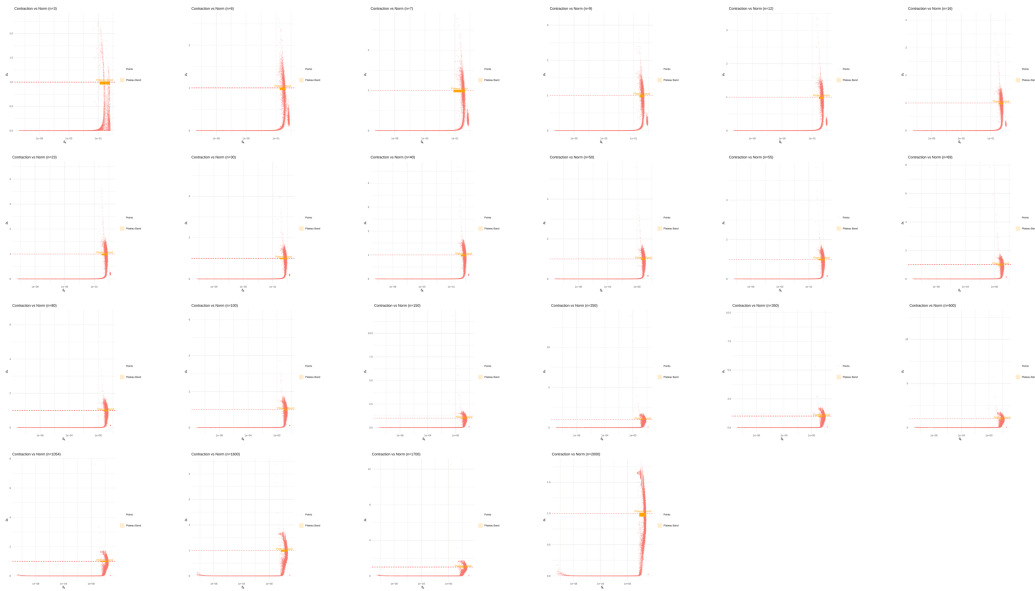


Figure 10: **Representative scatter plots of ρ_k versus Δ_k across matrix sizes.** The grid displays the scatter plots of (Δ_k, ρ_k) for all tested dimensions. For every size n , the points exhibit the same distinctive pattern: large values of Δ_k correspond to strong contraction ($\rho_k \ll 1$), while as $\Delta_k \rightarrow 0$ the values of ρ_k concentrate tightly near 1. The persistence of this structure across all dimensions shows that the overshoot behavior is essentially independent of matrix size.

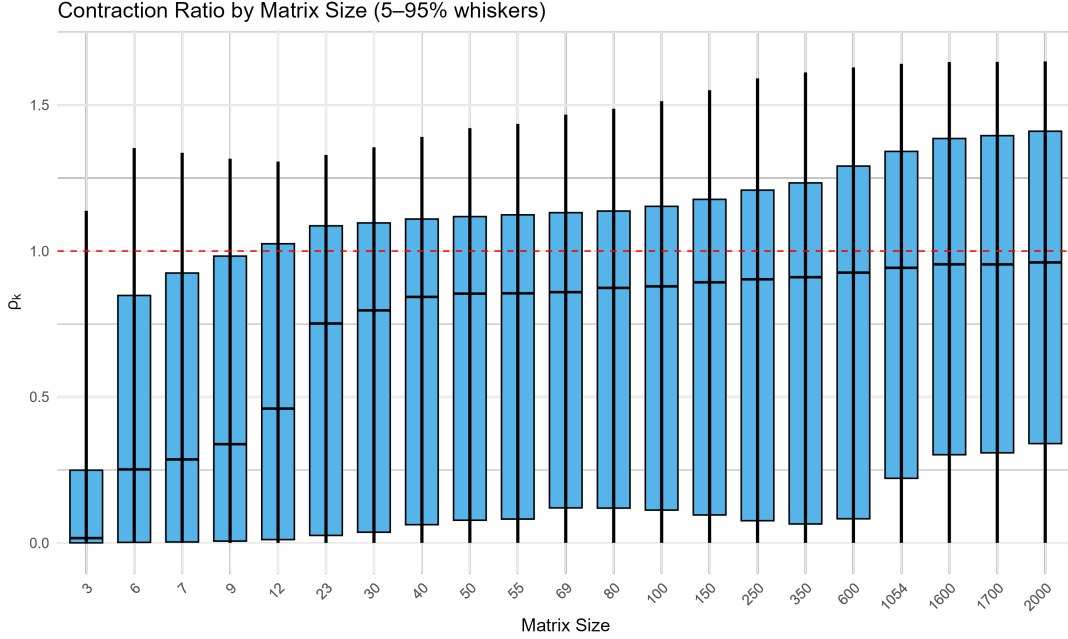


Figure 11: **Contraction ratios $\rho_k = \Delta_{k+1}/\Delta_k$ across matrix sizes (5–95% whiskers)**. For each dimension n , the box shows the interquartile range $[Q_{0.25}, Q_{0.75}]$, with the thick bar indicating the median $Q_{0.50}$; vertical whiskers correspond to the $Q_{0.05}$ and $Q_{0.95}$ quantiles. The dashed line $y = 1$ marks perfect isometry. Medians lie close to 1, indicating that, after the first iteration, most steps are non-expansive or nearly isometric. The interquartile ranges remain uniformly narrow across all sizes, and the 95% whiskers stay close to 1, showing that the overshoot behavior is consistently small and largely independent of dimension.

every trajectory

$$V_\infty = \sum_{k \geq 0} \Delta_k, \quad (6.5)$$

is finite in all 22,000+ trials.

Consistently with the heuristic scaling $\Delta_0 = O(n)$ in Law I and the uniformly bounded number of subsequent iterations in Law IV, the total variation grows approximately linearly with the dimension: its median is about $2.3n$ in Frobenius norm across the tested range (from roughly 4.5 for $n = 3$ to about 4.6×10^3 for $n = 2000$; see Table 2).

Table 2: Empirical distribution of the total variation $V_\infty = \sum_{k \geq 0} \Delta_k$ (Frobenius norm) across all trials for selected dimensions.

n	Median	95th Percentile	99th Percentile	Max
3	4.5	6.8	9.3	9.3
100	217	256	286	312
600	1360	1540	1660	1801
2000	4580	5220	5580	6020

This linear growth — dominated by the initial contraction — is fully consistent with the theoretical scaling from Law I and the bounded iteration count that will be explored with Law IV.

Total variation along trajectories. For each dimension n and trial t , the cumulative change along the trajectory is measured by the total variation

$$V_\infty^{(t)}(n) = \sum_{k \geq 0} \Delta_k^{(t)}.$$

Figure 12 displays boxplots of $V_\infty^{(t)}(n)$ over $N = 1000$ trials for every tested size. The total variation is finite in every run and grows approximately linearly with n : the median $V_\infty^{(t)}(n)$ increases from about 4.5 at $n = 3$ to about 4.6×10^3 at $n = 2000$, with relatively narrow interquartile bands around each median and maxima below 5.4×10^3 across all trials. Thus, although the cumulative motion is dimension-dependent, it remains quantitatively controlled and exhibits no sign of divergence.

Taken together, these observations show that the iteration settles into a remarkably stable regime: oscillations remain uniformly bounded across all tested dimensions, and the values of ρ_k concentrate in an increasingly tight band as $\Delta_k \rightarrow 0$. Decay progresses in a highly regulated fashion, with no runaway growth or irregular bursts—only a controlled descent that is effectively dimension-independent. This degree of regularity is striking for a nonlinear map with no *a priori* monotonicity guarantees, and it reveals a structural coherence that any future analytical theory must account for.

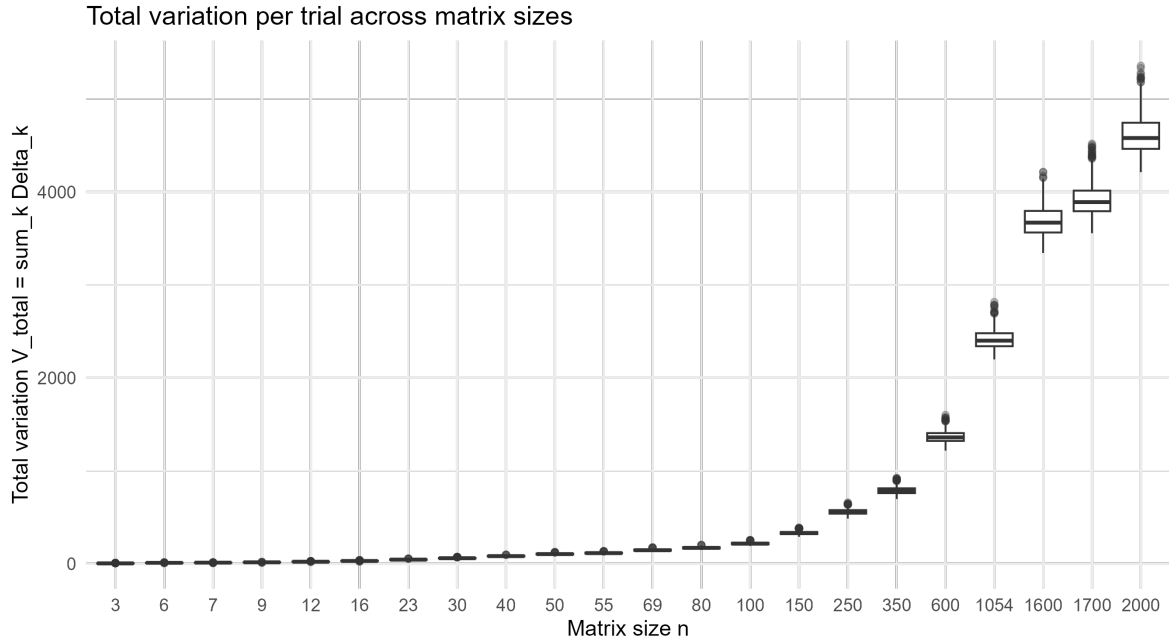


Figure 12: **Total variation** $V_\infty^{(t)}(n) = \sum_k \Delta_k^{(t)}$ **by matrix size.** Boxplots over $N = 1000$ trials per size. The total variation is finite in every trajectory and grows roughly linearly with n . Interquartile ranges remain narrow relative to the median at each dimension, indicating stable behavior across trials.

6.3 Law III: Dimension-independent contraction law

The third empirical law describes how the instantaneous contraction ratio $\rho_k := \Delta_{k+1}/\Delta_k$ depends on the step magnitude Δ_k . Across all tested matrix sizes, trials, and random initializations, the cloud of points (Δ_k, ρ_k) exhibits the same characteristic *V-shaped* organization in the (Δ_k, ρ_k) -plane. This structure, together with its overshoots, is an empirical finding of the numerical study.

Binned median contraction curves. For each matrix size n , all observed pairs (Δ_k, ρ_k) from all trials are collected. The values of Δ_k are partitioned into logarithmic bins $\{\mathcal{B}_b\}$. Within each bin we compute the median step magnitude and the corresponding median contraction ratio

$$\delta_b := \text{median}\{\Delta_k : \Delta_k \in \mathcal{B}_b\}, \quad \bar{\rho}_n(\delta_b) := \text{median}\{\rho_k : \Delta_k \in \mathcal{B}_b\}, \quad (6.6)$$

together with the 10th and 90th percentiles of ρ_k in that bin. The map $\delta_b \mapsto \bar{\rho}_n(\delta_b)$ summarizes, for a fixed dimension n , how the contraction ratio varies as a function of the current step size. The 10th–90th percentile band records the typical spread of ρ_k around its median, including overshoots $\rho_k > 1$.

Empirical Law III (Universal dimension-independent contraction). *Across all dimensions $n \in \{3, \dots, 2000\}$, the curves $\delta_b \mapsto \bar{\rho}_n(\delta_b)$ and their 10th–90th percentile bands exhibit the following empirical features:*

1. **Strong contraction for large steps.** *For large δ_b (corresponding to early iterations), the median contraction ratios satisfy $\bar{\rho}_n(\delta_b) \ll 1$, and the 10th–90th percentile band lies well below 1. Large steps are typically followed by much smaller steps.*
2. **Near-isometry with small overshoots for small steps.** *As $\delta_b \downarrow 0$, one observes*

$$\bar{\rho}_n(\delta_b) \longrightarrow 1,$$

and the 10th–90th percentile band becomes a narrow strip around 1. Both $\rho_k < 1$ and $\rho_k > 1$ occur, but overshoots $\rho_k > 1$ remain small: their magnitude decreases with δ_b , and the envelope width shrinks as $\delta_b \downarrow 0$.

3. **Dimension-independence and V-shape.** *When the curves $\delta_b \mapsto \bar{\rho}_n(\delta_b)$ are plotted for all tested sizes, they lie almost exactly on top of one another. The combined graph forms a V-shaped pattern: a contractive branch with $\bar{\rho}_n(\delta_b) \ll 1$ at large δ_b , and a near-horizontal, near-isometric branch with $\bar{\rho}_n(\delta_b) \approx 1$ and small overshoots at small δ_b , with no visible dependence on n .*

Overshoots and spread. The 10th–90th percentile band around $\bar{\rho}_n(\delta_b)$ provides a quantitative description of overshoots. For intermediate and small step sizes, the band typically straddles the line $\rho = 1$, indicating that both slight contractions and slight expansions occur from one step to the next. As $\delta_b \downarrow 0$, this band contracts to a narrow interval around 1, so overshoots $\rho_k > 1$ are present but uniformly small. When all sizes are pooled before binning, the same pattern is observed: the median curve and its envelope depend primarily on Δ_k , not on the matrix dimension.

Interpretation and discussion. The organization of (Δ_k, ρ_k) into a V-shaped pattern, together with the shrinking overshoot band as $\Delta_k \downarrow 0$, is consistent with the geometric structure described in Subsection 4.4, but is established here only at the empirical level. Large step sizes Δ_k occur when the iterate is still far from satisfying the row-wise mean-zero and unit-norm conditions; in this regime, centering and normalization cause substantial changes to the rows, producing ratios $\rho_k \ll 1$. Once the rows lie close to the unit sphere in $\mathbf{1}^\perp$, the update moves mainly within the manifold \mathcal{M}_n , so Δ_{k+1} stays close to Δ_k and $\rho_k \approx 1$, with only small overshoots above and below unity. The resulting V-shape with a narrow overshoot band at small Δ_k is therefore a quantitative empirical signature of two regimes of the iteration: a contractive regime when the rows lie far from the manifold \mathcal{M}_n , and a near-isometric regime with small, bounded oscillations once they lie close to it. This universal dimension-independent structure is one of the central empirical findings of the study.

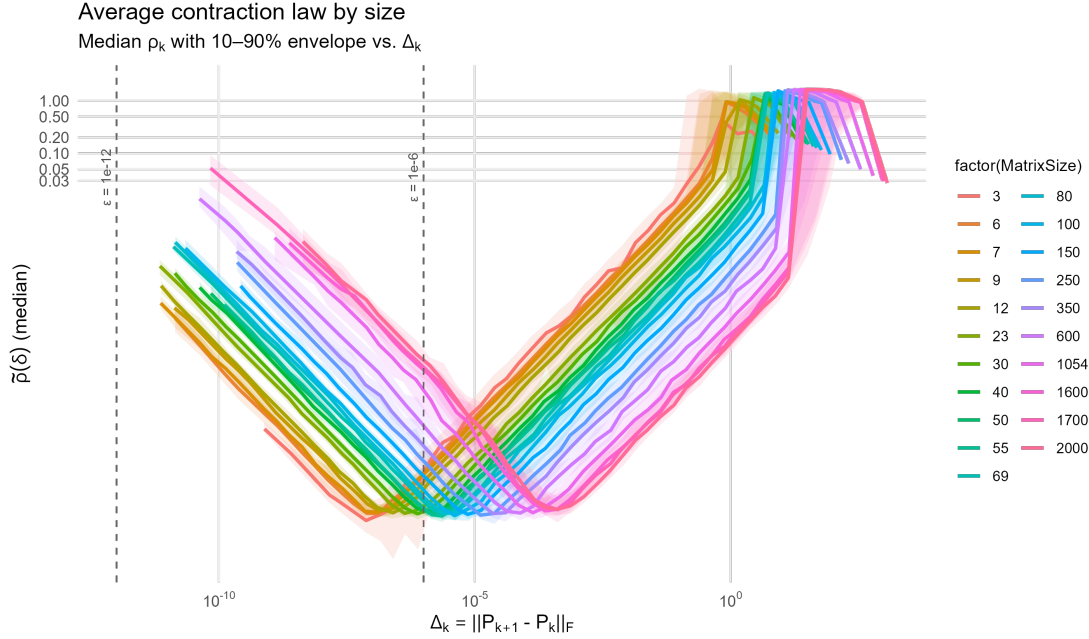


Figure 13: **Binned median contraction ratio by matrix size.** For each dimension n , the curve shows the binned median $\bar{\rho}_n(\delta_b)$ from (6.6), and the shaded ribbon indicates the 10th–90th percentile range of ρ_k within each bin of Δ_k . For large δ_b , medians satisfy $\bar{\rho}_n(\delta_b) \ll 1$ and the ribbon lies well below 1, while for small δ_b the medians approach 1 and the ribbon becomes a narrow band around 1. The curves and ribbons for different n nearly coincide, showing that the observed ρ_k – Δ_k behavior, including overshoots, is empirically dimension-independent.

6.4 Law IV: Uniformly bounded iteration counts

For a fixed tolerance $\varepsilon > 0$, the convergence time is defined in (5.2) by

$$T(n, \varepsilon) := \min \left\{ k \in \mathbb{N} : \Delta_j < \varepsilon \text{ for all } j \geq k \right\}, \quad \Delta_k = \|P_{k+1} - P_k\|_F.$$

From $N = 1000$ independent trials at each size n , samples $T_1(n, \varepsilon), \dots, T_N(n, \varepsilon)$ are obtained.

Empirical Law IV (Bounded iteration counts). *For each fixed $\varepsilon > 0$, the distribution of $T(n, \varepsilon)$ remains in a tight, dimension-independent band. The median and upper quantiles (including the 90% and 95% quantiles), the mean $\mu(n) := \mathbb{E}[T(n, \varepsilon)]$, and the standard deviation $\sigma(n) := \sqrt{\text{Var}(T(n, \varepsilon))}$ are all uniformly bounded in n . Equivalently,*

$$\sup_n \text{med}(T(n, \varepsilon)) < \infty, \quad \sup_n Q_{0.95}(T(n, \varepsilon)) < \infty, \quad \sup_n \mu(n) < \infty, \quad \sup_n \sigma(n) < \infty.$$

For each dimension n and $N = 1000$ random initializations $P_0^{(t)}$, the first k satisfying $\Delta_j^{(t)} < \varepsilon$ for all $j \geq k$ is recorded. The per-size statistics

$$\mu(n) = \frac{1}{N} \sum_t T_t(n, \varepsilon), \quad \sigma(n) = \sqrt{\frac{1}{N-1} \sum_t (T_t(n, \varepsilon) - \mu(n))^2}, \quad F_n(k) = \frac{1}{N} \sum_t \mathbf{1}\{T_t(n, \varepsilon) \leq k\}.$$

are then computed. The boundedness of $\mu(n)$, $\sigma(n)$, and high quantiles of $F_n(k)$ across all n supports Law IV.

Empirically, Law II shows that $\rho_k = \Delta_{k+1}/\Delta_k$ concentrates near 1, with diminishing overshoot as $\Delta_k \rightarrow 0$. In practice this produces a small but persistent negative drift in $\log \Delta_k$, up to bounded fluctuations, which matches the uniformly bounded convergence times observed across all dimensions.

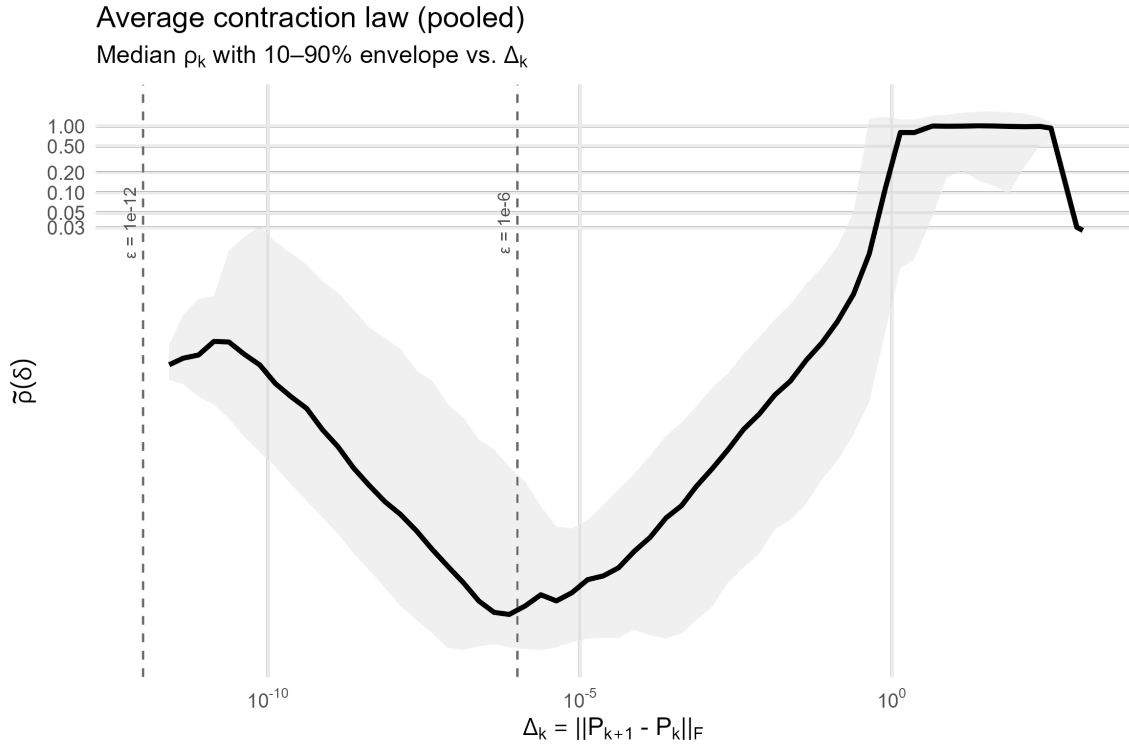


Figure 14: **Pooled binned median contraction law.** All pairs (Δ_k, ρ_k) from all sizes are pooled and binned in Δ_k . The curve shows the binned median contraction ratio $\bar{\rho}(\delta_b)$, and the ribbon shows the 10th–90th percentile range. The pooled median and envelope reproduce the same V-shaped structure as in Figure 13: strong contraction at large δ_b , near-isometry with small overshoots at small δ_b , and a narrow spread around $\rho = 1$ in the small-step regime.

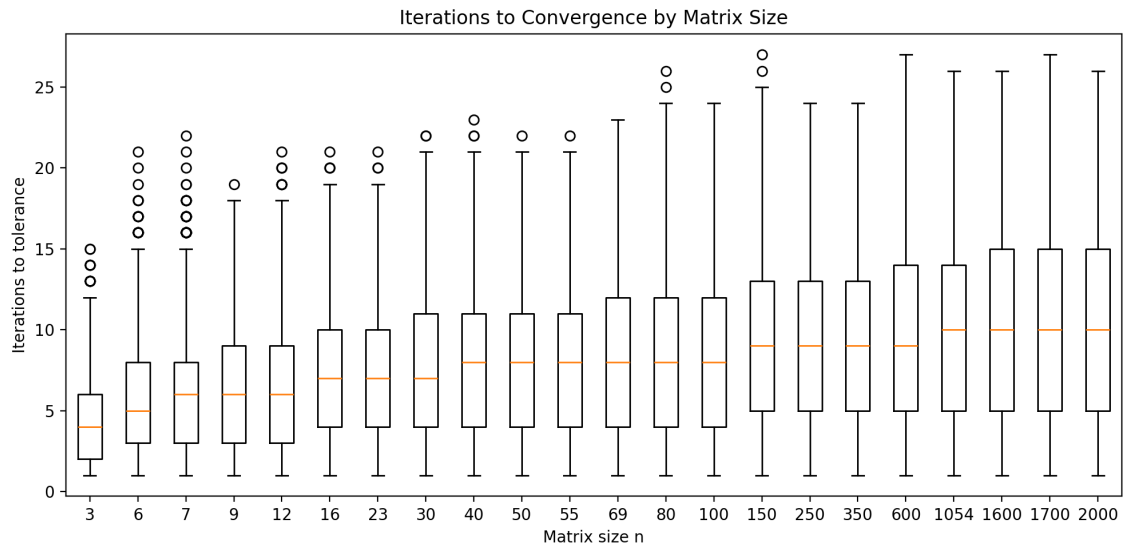


Figure 15: **Convergence time $T(n, \varepsilon)$ across sizes (boxplots; $N = 1000$ trials per size).** For each n , the box shows the interquartile range of $T(n, \varepsilon)$, the central line is the median, whiskers mark the bulk, and points are outliers. The whisker band remains in a narrow range, here approximately between five and twenty iterations, with rare outliers below twenty-five. The width of this band does not grow with n , which is direct distributional evidence that $T(n, \varepsilon)$ is uniformly bounded in the matrix size.

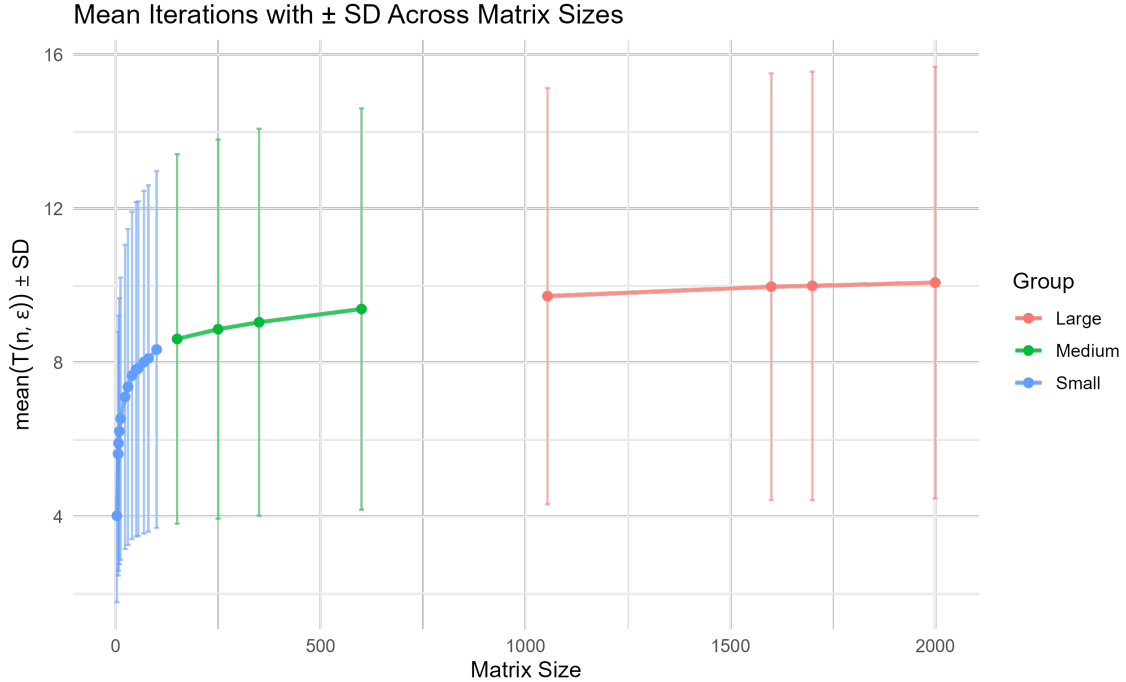


Figure 16: **Mean iterations $\mu(n)$ with $\pm\sigma(n)$ error bars, grouped by size.** From $N = 1000$ trials per size, $\mu(n) = \frac{1}{N} \sum_{i=1}^N T_i(n, \varepsilon)$ and $\sigma(n) = \sqrt{\frac{1}{N-1} \sum_{i=1}^N (T_i(n, \varepsilon) - \mu(n))^2}$. Both $\mu(n)$ and $\sigma(n)$ remain uniformly bounded and show no growth trend with n . This second-moment view corroborates the boxplot evidence that $T(n, \varepsilon)$ is of order one uniformly in n .

Table 3: Maximum observed iteration count $T_{\max}(n)$ over $N = 1000$ trials per dimension for $\varepsilon = 10^{-12}$. The maximum number of steps never exceeds 28 across the entire range $n \in [3, 2000]$, demonstrating dimension-independent convergence time.

n	$T_{\max}(n)$	n	$T_{\max}(n)$	n	$T_{\max}(n)$	n	$T_{\max}(n)$
3	15	16	22	69	25	350	27
6	21	23	23	80	25	600	27
7	22	30	23	100	25	1054	28
9	19	40	24	150	26	1600	28
12	21	50	24	250	26	1700	28
55	24	2000	28				

As Table 3 shows, the iteration never exceeds 28 steps in any of the 22,000 trials across dimensions $n \in [3, 2000]$, providing definitive numerical evidence that the convergence time is of order $O(1)$, entirely independent of dimension.

The uniform boundedness of the iteration count contrasts with many linear scaling procedures such as Sinkhorn’s convex normalization [14], whose iteration counts typically increase with dimension. The universality of $T(n, \varepsilon)$ supports the finite boundedness of the cumulative variation defined in Equation (6.5), whose value remains finite in all experiments. Moreover, while V_∞ grows approximately linearly with n , its distribution at each fixed dimension is tightly concentrated around its median.

7 Summary and Interpretation of the Empirical Laws

The four empirical laws established in Section 6 provide a coherent description of the global behavior of the iteration $P_{k+1} = f(P_k)$. Each law is based on simple diagnostics yet together

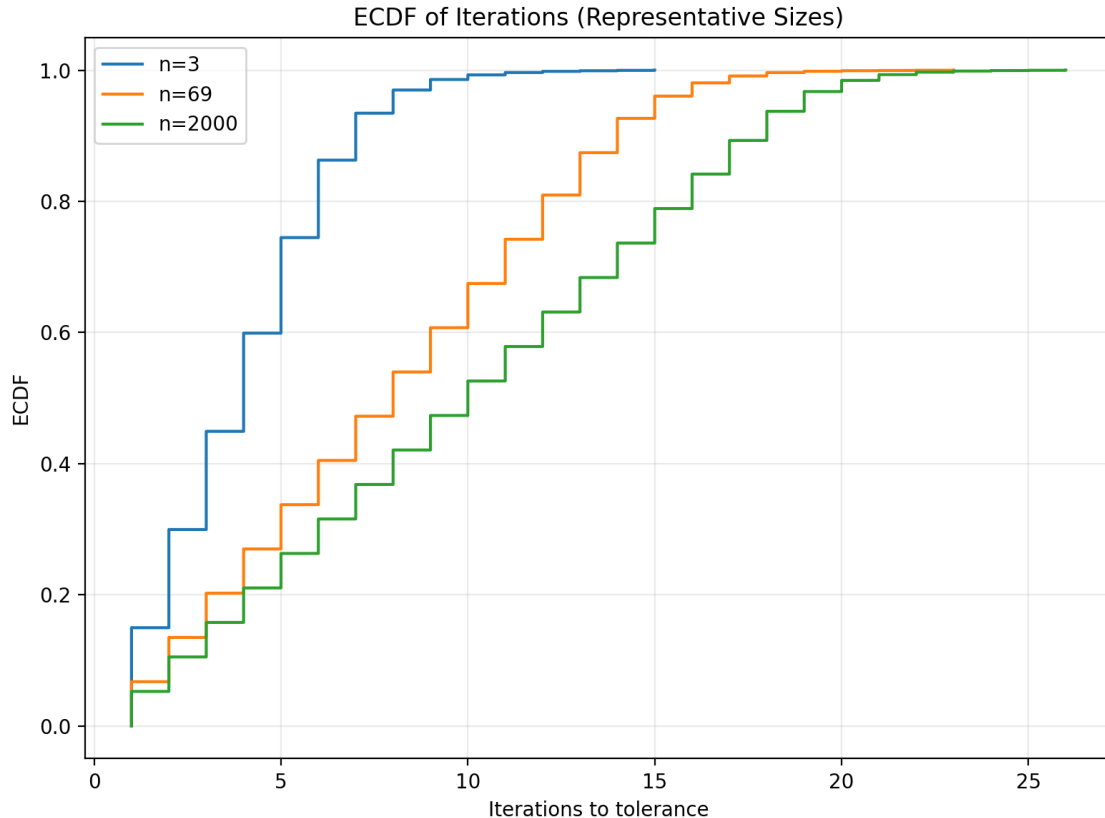


Figure 17: **Empirical distribution functions of iteration counts at representative sizes.** For each n , the empirical distribution function $F_n(k) = \frac{1}{N} \sum_{i=1}^N \mathbf{1}\{T_i(n, \varepsilon) \leq k\}$ rises steeply and saturates rapidly. In the runs shown, the 90% quantile occurs by $k = 7$ for $n = 3$, by $k = 15$ for $n = 69$, and by $k = 20$ for $n = 2000$. Almost all trajectories therefore terminate within a small number of steps, independent of dimension.

they reveal a stable, dimension-independent structure across all tested sizes. This empirical stability was already observed in the classical clustering literature [4, 11], and implicitly underlies Kruskal’s original CONCOR convergence report [8].

Law I shows that the first update $P_0 \mapsto P_1$ produces a sharp reduction in the Frobenius step size, with contraction ratio $\rho_0 = \Delta_1/\Delta_0$ far below 1 and essentially independent of the matrix size. This reflects the fact that centering removes a large common component of each row along $\mathbf{1}$, and normalization enforces unit length, jointly inducing a strong corrective motion toward the mean-zero, unit-norm row structure imposed by the correlation operator.

Law II shows that, after the initial drop, the sequence Δ_k decays in a nearly monotone fashion, with small overshoots that remain uniformly bounded across dimensions and diminish as the iteration progresses. Although no analytical proof of finite total variation is known, the empirical behavior points strongly in that direction. Indeed, across all dimensions, the total variation

$$V_\infty = \sum_{k \geq 0} \Delta_k$$

is finite in every trial and for every trajectory and grows approximately linearly with n , with narrow interquartile ranges at each dimension.

Law III shows that the one-step contraction ratio ρ_k depends almost exclusively on the current step size Δ_k . Large steps correspond to strong contraction, while very small steps correspond to near-isometric behavior. When pooled across all sizes and trials, the points (Δ_k, ρ_k) align

along the same characteristic V-shaped curve, with a narrow band of overshoot around 1 in the small-step regime. Once Δ_k is specified, the dimension plays no further role. The large-step branch reflects strong correction of deviations transverse to the row-spherical manifold \mathcal{M}_n , whereas the small-step branch reflects the nearly tangential motion of the iteration when the rows already lie close to \mathcal{M}_n .

Law IV shows that, for any fixed tolerance $\varepsilon > 0$, the number of iterations $T(n, \varepsilon)$ required for stabilization remains tightly bounded across all matrix sizes. This is consistent with the eventual negative drift of $\log \Delta_k$ suggested by Law II and with the universal ρ - Δ relationship of Law III. Empirically, almost all trajectories stabilize in a small, dimension-independent number of steps, even for the largest matrices tested.

Taken together, the four laws reveal a geometric picture of the composite map $f = \Phi \circ \Psi$. The centering-normalization step pushes the iterate sharply toward the underlying row-spherical geometry and heavily damps deviations transverse to it. Once the rows lie close to this geometry, the dynamics become almost tangential, producing small, stable steps whose behavior is accurately captured by the universal V-shaped contraction law. The Gram map transfers these changes to the correlation matrix without introducing dimension-dependent distortions, explaining the strong initial drop, the slow and controlled decay that follows, and the dimension-independent behavior of all quantitative measures.

A closer examination of the cumulative step length $V_\infty = \sum_{k \geq 0} \Delta_k$ reveals an additional geometric feature of the iteration. For every tested dimension, V_∞ is finite, in agreement with the near-monotone decay of Δ_k and the bounded overshoot behavior of Law II. However, unlike the iteration count $T(n, \varepsilon)$ of Law IV, the total variation is *not* dimension-independent. Empirically, V_∞ grows with n in an approximately linear fashion, $V_\infty \approx Cn$ with $C \approx 2.3$, while remaining tightly concentrated around its median at each dimension.

This behavior reflects the geometry of the row-spherical manifold

$$\mathcal{M}_n = \{Z \in \mathbb{R}^{n \times n} : \mathbf{1}^\top Z(i, :) = 0, \|Z(i, :)\|_2 = 1 \text{ for all } i\},$$

onto which the operator Ψ maps each centered row of P_k . For large n , the initial matrix P_0 typically lies farther from \mathcal{M}_n in Frobenius distance, because its rows deviate more substantially—in both mean and magnitude—from the unit sphere contained in $\mathbf{1}^\perp$. The early iterations therefore traverse a longer path in the ambient space. Once the iterate approaches \mathcal{M}_n , however, the dynamics enter the near-isometric regime documented in Law III, and the number of subsequent corrective steps remains uniformly bounded in n .

Thus, the scaling of V_∞ with dimension reflects a clear geometric separation: the *distance* from the initial state to the row-spherical manifold \mathcal{M}_n increases with n , but the *number of steps* required to reach and remain near \mathcal{M}_n does not. This reconciles the growth of V_∞ with the striking dimension-independence seen in Laws III and IV.

The empirical laws also clarify why convergence has been consistently observed since the early work of McQuitty, Breiger–Boorman–Arabie, and Chen. The map is strongly contracting in directions that alter row means or row norms, and nearly isometric along directions tangent to the mean-zero, unit-norm row manifold. This dual behavior is straightforward to verify locally but challenging to analyze globally due to nonlinearity and the structure of the fixed-point set of block- $\{\pm 1\}$ patterns. Despite these difficulties, the empirical laws demonstrate that the iteration behaves regularly across all dimensions and admits stable patterns of contraction, overshoot control, and convergence time.

The main theoretical challenge is to convert these empirical regularities into uniform estimates valid for all initial matrices. Law II suggests a Lyapunov-type structure with finite total variation, and Law III provides a precise functional dependence between Δ_k and ρ_k that any future theory must explain. Establishing such properties analytically would close a long-standing gap in the understanding of iterated correlation maps and complete the convergence picture initiated in the earlier literature.

7.1 Why global convergence has remained an open problem

The empirical evidence presented in this work—four sharp, dimension-independent regularities that hold uniformly up to dimension $n = 2000$ —reveals a degree of order that appears almost too good to be true for a nonlinear iteration. Yet, despite more than fifty years of consistent empirical success across psychometrics, social-network analysis, and data visualization, no proof of global convergence from arbitrary initial conditions has ever been published. At first sight, standard fixed-point theorems might seem applicable. Brouwer’s theorem guarantees that the continuous map f has at least one fixed point on the compact, convex ellipsope \mathcal{E}_n . Moreover, if a global contraction bound

$$\|f(P) - f(Q)\|_F \leq c \|P - Q\|_F$$

held uniformly for all P, Q with some $c < 1$, then Banach’s contraction principle would immediately imply uniqueness of the fixed point and global convergence of the iteration $P_{k+1} = f(P_k)$. However, none of the hypotheses needed for such arguments are satisfied. The structural obstacles are decisive:

1. *The fixed-point set is finite, and determined by discrete block structure.* Kruskal (ca. 1965, as summarized in [4]) established that the only fixed points reachable by the iteration are block- $\{\pm 1\}$ correlation matrices: symmetric positive semidefinite matrices with unit diagonal whose off-diagonal entries are exactly $+1$ within blocks and -1 between blocks (up to row/column permutation and sign flips of entire blocks). This set $\mathcal{F}_n \subset \mathcal{E}_n$ is finite for each n , within the class of iterates reachable from nondegenerate initial conditions, and it grows exponentially with n . Although it lies inside the convex ellipsope \mathcal{E}_n of all correlation matrices, \mathcal{F}_n itself, was not fully characterized by [5, 8]. Consequently, virtually all global convergence frameworks that rely on convexity of the target set—Fejér monotonicity, proximal methods, or Bregman projections [3]—are inapplicable. A more systematic analysis of these algebraic fixed points is developed in the forthcoming work [2], but a complete characterization for general n remains open.
2. *The map is nonlinear and not uniformly contractive.* Law III demonstrates a near-isometric regime for small perturbations, so Banach’s contraction principle cannot be applied globally.
3. *The iteration is not a standard Mann-type averaging scheme.* Classical mean-value iteration methods [10] study convex combinations of a point with its image under a nonexpansive map. The correlation iteration applies the full nonlinear map f at each step without averaging and, moreover, lacks global nonexpansivity, so Mann-type convergence results cannot be invoked directly.
4. *Contraction is strongly anisotropic.* The iteration contracts aggressively in directions that alter row means or row norms (Law I and the transverse branch of Law III), but is nearly isometric along directions tangent to the mean-zero, unit-norm row manifold (the tangential branch of Law III). No known metric turns the map into a uniform contraction on the whole space.
5. *Sinkhorn-type arguments fail.* Sinkhorn–Knopp scaling converges globally because the target set (doubly-stochastic matrices) is convex and the map is a contraction in Hilbert’s projective metric [14]. Here the effective target is the discrete set \mathcal{F}_n , and no analogous metric exists.

Kruskal’s local linearization shows that, once sufficiently close to any individual block- $\{\pm 1\}$ fixed point, convergence to that exact point is geometrically fast with spectral radius strictly smaller than 1 [4]. However, the global trajectory from a generic initial matrix must cross regions

far from all fixed points, and the basins of attraction of the exponentially many fixed points remain unknown.

The four empirical laws reported here are therefore all the more remarkable: they reveal that the dynamics are extraordinarily regular and essentially dimension-independent *despite* the severe structural barriers above. They constitute the first quantitative, global portrait of the correlation iteration and provide the precise, testable benchmarks that any future analytical convergence proof must reproduce.

8 Discussion and open problems

The empirical laws presented above clarify several structural properties of the iteration but also highlight what remains to be proved. Several open mathematical problems are listed here.

Global convergence. Classical local arguments support near-pattern geometric convergence, but a complete convergence theorem valid for all initializations and all dimensions is not available.

Finite total variation. Empirically, the sum of step sizes $\sum_k \Delta_k$ is finite for every trajectory and grows approximately linearly with the dimension, $V_\infty \approx Cn$. A proof would require showing that overshoots remain uniformly bounded and that the effective contraction ratio eventually drops below unity on average, together with a global upper bound of order $O(n)$.

Uniform control of overshoots. Law II shows that overshoots are small and bounded across all sizes. A theoretical explanation of this phenomenon is missing and would likely require a detailed study of the geometry of the centering and normalization maps.

Universal contraction law. Law III identifies a dimension-independent relation between the step size Δ_k and the ratio ρ_k . Understanding why this V-shaped profile emerges and why it is independent of n is an open analytical question.

Characterization of fixed points. The fixed-point set consists of block- $\{\pm 1\}$ correlation patterns. A detailed analysis of these fixed points, including stability properties and basins of attraction, is developed in the preprint [2].

Lyapunov functions. The iteration appears to admit a Lyapunov structure with strong contraction in directions orthogonal to the row-spherical manifold \mathcal{M}_n and near-isometry along directions tangent to \mathcal{M}_n , together with finite cumulative change. Constructing such a function explicitly remains an open challenge.

Dimension-independence. Many observed properties—first-step contraction, overshoot bounds, convergence time—are stable in n . Explaining this independence analytically is a key theoretical question.

The empirical laws identified here therefore supply the structural benchmarks that any full analytical theory must reproduce, and they delineate a precise pathway toward resolving a problem that has remained open since the 1960s.

References

- [1] I. AlHajj Hassan. *Computational Framework for Experiments on Iterated Correlation Matrices*. Zenodo, 2025. <https://doi.org/10.5281/zenodo.17794063>.

- [2] I. AlHajj Hassan and P. Zusmanovich. “Fixed points of iterated correlation matrices.” Preprint, 2025.
- [3] H. H. Bauschke and P. L. Combettes. *Convex Analysis and Monotone Operator Theory in Hilbert Spaces*, 2nd edition. Springer, 2017. <https://doi.org/10.1007/978-3-319-48311-5>.
- [4] R. L. Breiger, S. A. Boorman, and P. Arabie. An algorithm for clustering relational data with applications to social network analysis and comparison with multidimensional scaling. *Journal of Mathematical Psychology*, 12(3):328–383, 1975. [https://doi.org/10.1016/0022-2496\(75\)90028-0](https://doi.org/10.1016/0022-2496(75)90028-0)[https://doi.org/10.1016/0022-2496\(75\)90028-0](https://doi.org/10.1016/0022-2496(75)90028-0).
- [5] C.-C. Chen. Generalized association plots: Information visualization via iteratively generated correlation matrices. *Statistica Sinica*, 12(1):7–29, 2002. <http://www3.stat.sinica.edu.tw/statistica/http://www3.stat.sinica.edu.tw/statistica/>.
- [6] K. Goebel and W. A. Kirk. *Topics in Metric Fixed Point Theory*. Cambridge University Press, 1990. <https://doi.org/10.1017/CBO9780511526152><https://doi.org/10.1017/CBO9780511526152>.
- [7] L. Huang, D. Yang, and B. Lang. Iterative normalization: Beyond standardization towards efficient whitening. In *Proceedings of the IEEE Conference on Computer Vision and Pattern Recognition (CVPR)*, pages 4874–4883, 2019. https://openaccess.thecvf.com/content_CVPR_2019/html/Huang_Iterative_Normalization_Beyond_Standardization_Towards_Efficient_Whitening_CVPR_2019_paper.htmlOpenAccess: CVPR 2019.
- [8] J. B. Kruskal. A theorem about CONCOR. Technical Report MH 2C–571, Bell Laboratories, Murray Hill, NJ, 1978.
- [9] M. Laurent and S. Poljak. On the facial structure of the set of correlation matrices. *SIAM Journal on Matrix Analysis and Applications*, 17(2):530–547, 1996. <https://doi.org/10.1137/S089547989325030X><https://doi.org/10.1137/S089547989325030X>.
- [10] W. R. Mann. Mean value methods in iteration. *Proceedings of the American Mathematical Society*, 4(3):506–510, 1953. <https://doi.org/10.1090/S0002-9939-1953-0054846-3><https://doi.org/10.1090/S0002-9939-1953-0054846-3>.
- [11] L. L. McQuitty. Multiple clustering revisited: Comments, comparisons, new approaches. *Multivariate Behavioral Research*, 3(4):431–479, 1968. https://doi.org/10.1207/s15327906mbr0304_1.
- [12] Z. Opial. Weak convergence of the sequence of successive approximations for nonexpansive mappings. *Bulletin of the American Mathematical Society*, 73(4):591–597, 1967. <https://doi.org/10.1090/S0002-9904-1967-11761-0><https://doi.org/10.1090/S0002-9904-1967-11761-0>.
- [13] J. Saunderson, V. Chandrasekaran, P. A. Parrilo, and A. S. Willsky. Diagonal and low-rank matrix decompositions, correlation matrices, and ellipsoid fitting. *SIAM Journal on Matrix Analysis and Applications*, 33(3):813–839, 2012. <https://doi.org/10.1137/110837851><https://doi.org/10.1137/110837851>.
- [14] R. Sinkhorn. A relationship between arbitrary positive matrices and doubly stochastic matrices. *The Annals of Mathematical Statistics*, 35(2):876–879, 1964. <https://doi.org/10.1214/aoms/1177703599><https://doi.org/10.1214/aoms/1177703599>.